
Effect of the Amorphisation of Zeolitic Imidazole Frameworks on the Electrochemical Performance of Anodes

Master Thesis
Wessel Winters

Aalborg University
Department of Chemistry and Bioscience
Fredrik Bajers Vej 7H
DK-9220 Aalborg

Titel:

Effect of the Amorphisation of Zeolitic Imidazole Frameworks on the Electrochemical Performance of Anodes

Tema:

Metal-Organic Frameworks
Lithium Ion Batteries

Projektperiode:

Spring Semester 2021

Projektgruppe:

N/A

Deltager(e):

Wessel Winters

Vejleder(e):

Yuanzheng Yue
Chengwei Gao

Oplagstal: 1

Sidetale: 73

Afleveringsdato:

August 2, 2021

Abstract:

ZIF-62(Co) and ZIF-67 were synthesised and turned amorphous through melt-quenching and ball-milling respectively. The resulting materials were tested for their electrochemical performance with Galvanostatic charge-discharge tests, EIS and CV. The samples were further characterised with XRD, DSC, XPS and IR to confirm and compare the physical and structural properties of the materials in relation to their electrochemical performance. The electrochemical performance of ZIF-67 was changed due to the ball-milling, and all samples showed an ability to recover the capacity that was lost during the first few cycles.

Nomenclature

<i>Abbreviation</i>	<i>Name</i>
EV	Electric vehicle
bIm	Benzimidazole
ICE	Internal combustion engine
dmbIm	5,6-Dimethylbenzimidazole
DMF	N,N'-dimethylformamide
DSC	differential scanning calorimetry
Im	Imidazole
LIB	Lithium ion Battery
LMB	Lithium metal Battery
MOF	Metal-organic framework
NMR	Nuclear magnetic resonance
mIm	2-methyl-imidazole
CCV	Closed circuit voltage
SRO	Short-range order
T_d	Decomposition temperature
T_g	Glass transition temperature
OCV	Open circuit voltage
T_m	Melting temperature
PXRD	Powder X-ray diffraction
PEL	Potential Energy Landscape
EIS	Electrochemical Impedance Spectroscopy
CE	Coulombic Efficiency
C_p	Isobaric heat capacity
H	Enthalpy
S	Entropy
G	Gibbs energy
ZIF	Zeolitic imidazolate framework

Contents

Contents	vii
1 Introduction	1
2 General Description of Lithium Ion Batteries	5
2.1 LIBs as Galvanic Cells	5
2.2 Capacity and Stability	7
2.3 Polarization and the Closed Circuit Voltage	15
3 Anode Development	19
3.1 Lithium Metal Anodes	19
3.2 Graphite Anodes	20
3.3 Metal Alloying Anodes	22
3.4 Conversion	24
3.5 Cobalt Based Anodes	26
3.6 Order-Disorder Materials	27
3.7 Zeolitic Imidazolate Frameworks as Anodes	28
4 Glass	33
4.1 Thermodynamics of Solids and the Amorphisation Process	33
4.2 Annealing and the Structure of Glass	35
4.3 Annealing of ZIF-62	36
4.4 Expected Changes in Electrochemical Performance	37
5 Electrochemical Characterisation Methods	39
5.1 Galvanostatic Charge-Discharge Cycling	39
5.2 Electrochemical Impedance Spectroscopy	40
5.3 Cyclic Voltammetry	43
6 Experimental Section	45
6.1 List of Instruments and Materials	45
6.2 ZIF-62(Co) Synthesis	45
6.3 ZIF-67 Synthesis	46
6.4 ZIF-62(Co) melt-quenching	46
6.5 ZIF-67 ball-milling	47
6.6 Powder X-ray Diffraction	47
6.7 Liquid Nuclear Magnetic Resonance Spectroscopy	47
6.8 Differential Scanning Calorimetry	47
6.9 Other	47
7 Results	49
7.1 Powder X-ray Diffraction	49

7.2	Scanning Electron Microscope	50
7.3	Proton-NMR	52
7.4	X-ray Photoelectron Spectroscopy	53
7.5	Differential Scanning Calorimetry	56
7.6	Cyclic Voltammetry	58
7.7	Galvanostatic Charge-Discharge Cycling	61
7.8	Electrochemical Impedance Spectroscopy	65
7.9	BET Surface Area	66
7.10	Fourier Transformed-Infrared Transmittance Spectroscopy	66
7.11	Discussion	67
7.12	Conclusion	68
	Bibliography	69

Introduction

1

Renewable energy and reducing the energy footprint are two of the most important research topics in the 21st century, not only to reduce the negative effects of climate change, but also to find alternatives to fossil fuels, which by virtue of their origin are bound to run dry at some point in the future. Because of this there has been a push towards improving green technology from the public and political spheres, which has only been increasing with the recent political regime change in America. While creating renewable energy is important, a difficult issue that has to be addressed is how to store energy once it is made. Having a stable baseline energy reserve is important to keep a national power grid running, not only from an energy standpoint, but also from an electrical frequency standpoint. Having too much energy can be harmful to electrical transformers, which means that the total electricity has to be carefully managed to meet immediate increases and decreases in demand for electricity. The main sources of renewable energy are hydro, solar and wind energy. The latter two fluctuate based on the weather, and the former is a unlikely candidate for further expansion due to geographic requirements. Fuel cells are a type of electrochemical cell that can help with this regard, where excess electrical energy is stored as chemical energy, and returned back as electrical energy at a later point, hopefully with minimal energy loss [1]. This way fluctuations in demand can easier be met. While fuel cells are not a hot topic in the public discourse, electric vehicles (EVs) have cemented themselves into the public consciousness as one of the primary ways to reduce CO₂ emissions. The electrochemical cells used to power the electric motors in EVs are Lithium ion batteries (LIBs), which initially were developed for wireless electronics, a market seemingly unrelated to renewable energy.

It is likely that EVs have gained popularity due to the messaging of how the combustion of gasoline and diesel in cars directly lead to CO₂ emissions. Cars are a daily necessity for many, and purchasing a EV can feel like a direct personal investment in reducing emissions. Life-cycle analysis related to EVs from a European Environment Agency report estimated that the emissions related to manufacturing and usage of EVs is reduced by 26% when compared to vehicles with a internal combustion engine (ICE) [2]. This is a sizable decrease considering that 27% of the total emissions come from the transport sector. The transport and logistics sector is one of the most important components of the global economy, and is not something that can be slowed down without economic consequences. The transport of labour to work in the form commuting and the transport of goods for consumption is what keeps the economy running on a daily basis. Currently trucks, ships and planes all run on non-renewable energy sources, in the form of liquid fuels with a high energy density [3] (as seen in table 1). While electric passenger cars can fulfil their intended purpose with a lower energy density fuel, the same does not apply for larger vehicles. Cargo-trucks and

ships have to travel long distances, and large passenger planes require high energy density fuels to reduce the overall weight during flight.

	<i>Gravimetric [MJ/kg]</i>	<i>Volumetric [MJ/L]</i>	<i>Volumetric Power [kWh/L]</i>
Gasoline	46	34	9500
Diesel	45	35	9700
Kerosene	43	34	9500
LIB	0.85	2.3	0.68

* Adjusting for efficiency of ICEs

Additionally refuelling processes and infrastructure have to be taken into consideration. To supply all the energy needs of vehicles through the currently existing power grid could be problematic without improvements in fuel cells or alternative energy storage technology. A recent example where large swings in electricity demands caused instability was in Texas, during a surprise cold wave, resulting in massive power outages, even with the baseline supplied by fossil fuels. Therefore further improvement to battery technology and manufacturing have to be made before can become able to stabilise and supply the large demand for energy.

The initial technological development of the LIB created a novel opportunity for EVs, made possible by the higher energy density when compared to older batteries. The contrast between figure 1.1 and table 1 sheds some light how EVs would not have been possible with older battery technology. LIBs are a strong improvement when compared to older batteries, and still lack the power density to perform as strong as liquid fossil fuels. While the numbers might seem in favour of keeping liquids fossil fuels, there are limitations to ICEs, such as a theoretical maximum efficiency of 40 % [4], whereas electric motors currently have an efficiency of 90 % [5]. This means that improvements in battery performance result in almost equal improvement in the performance of battery powered devices.

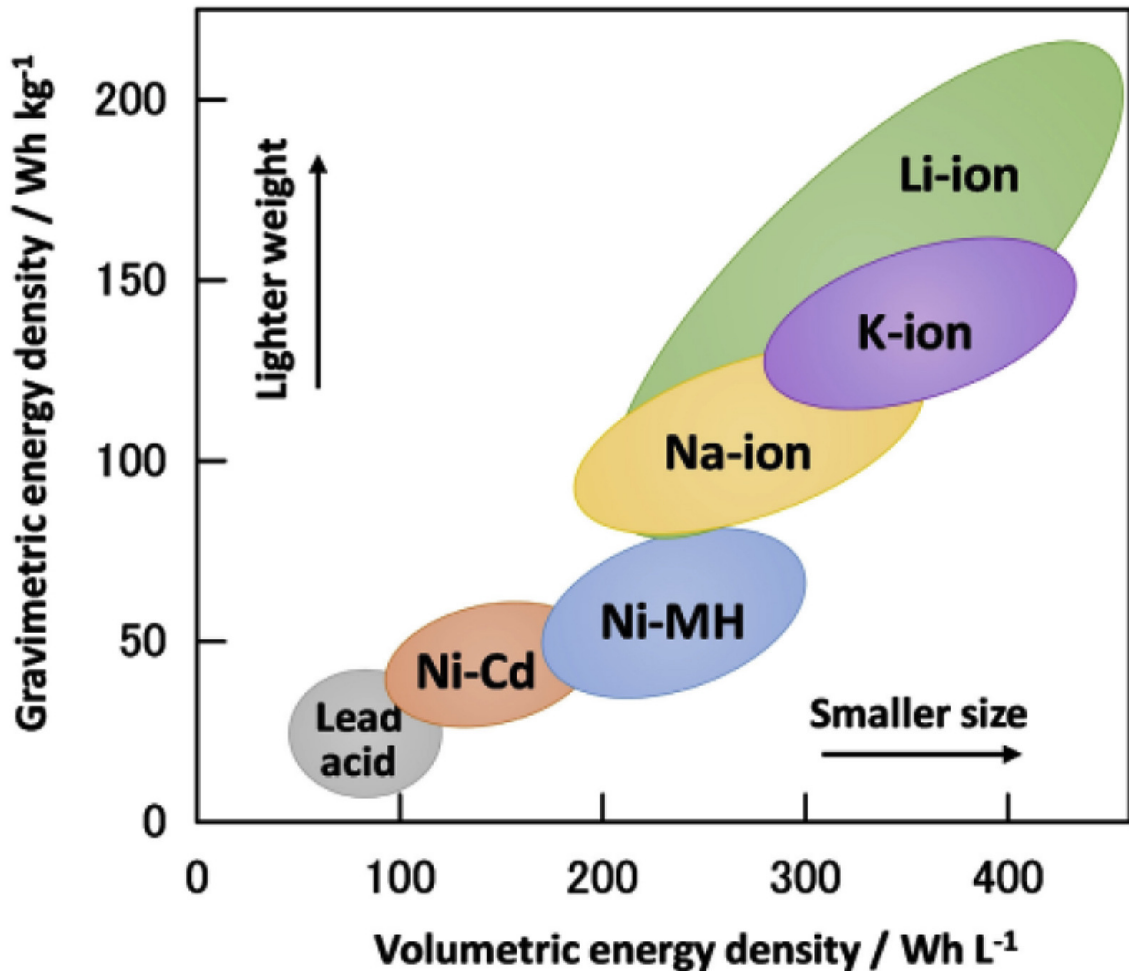


Figure 1.1: Comparison of the gravimetric energy density and the volumetric energy density of various battery types [6].

While the improvement on LIB technology is slowly coming along, questions about reliability and safety of the batteries is still a contention. Stories about self-igniting lithium batteries is not only a concern for EVs but also for smaller mobile devices. The cycling stability of LIBs is also important when it comes to consumer opinions, where there is confusion whether the decreasing battery life is inherent to the technology or caused by intentional design flaws. In the EV market, benefits such as lower maintenance and fuel cost are often mentioned, however, EVs are still considered to be a worse investment than a vehicle with a ICE, due to the battery degradation severely reducing the resell value of the vehicle. Safety and the lifetime of a battery are often related, which means that both issues can be addressed simultaneously. Although, often at the cost of energy density and power density. The balancing of these variables has been the center of LIB research since the first commercial LIBs were developed. Promising materials such as silicon (Si) similarly have issues where achieving high performance and good cycling stability at the same time is not yet possible [7]. Finding new solutions to improve performance without creating unsafe batteries is necessary to create a full shift towards batteries as primary form of portable energy.

There are many different angles when it comes to improving batteries. One of those

is gaining a better understanding of the order-disorder transitions have been observed in various electrode materials during the cycling process. V_2O_5 and TiO_2 are a couple of examples of materials that show a long term cycling stability. The performance of these materials is limited by other aspects such as power output and specific capacity and therefore have not gained as much attention as high-power experimental materials. However, the cycling stability of these materials is remarkable, as the capacity remains stable or even increases during cycling. This can significant when considering applications that require less power and are recharged often, such as small electronic devices. Having anodes that last longer also closer follow the first principle of reduce, reuse and recycle, compared to high power cells that cannot last as long. Understanding the mechanism of order-disorder transitions can also be relevant as an additional tool to potentially improve the performance of future novel materials.

Metal Organic Frameworks (MOF) have gained a lot of attention due to their various applications related to their large pore volume and chemical functionality [8]. Some of the more common applications of MOFs are as membranes, gas separation, catalyst, solid state ionic conductors and super-capacitors [9]. The latter two closely related to battery technology. MOFs have also been tested as anode materials, some of which have long term cycling stability and even increasing capacity with each cycle [10, 11]. The goal of this thesis will be the characterisation of ZIF-62(Co) and ZIF-67, two MOFs belonging to the Zeolitic Imidazole Framework (ZIF) subgroup. Their performance as anode materials will be tested to understand the connection between the structural features of the two ZIFs and amorphous variants of both, the electrochemical performance and if it is related to a order-disorder transition.

General Description of Lithium Ion Batteries 2

This chapter focuses on the properties of batteries that determine the performance. Describing the most relevant aspects of how the components interact, and how the physical and chemical properties of those components affect the performance of the battery. The focus will remain on anodes, only considering cathodes and electrolytes when relevant.

2.1 LIBs as Galvanic Cells

The term battery stems from an array of galvanic cells, where currently the terms battery or cell are used almost interchangeably for a single galvanic cell. The galvanic cell is able to convert chemical potential energy into an electrical current. An electrolytic cell is the opposite, using electrical current to drive a non-spontaneous reaction. Although for modern rechargeable batteries, they act as both a galvanic cell during discharging and as an electrolytic cell during charging. The galvanic cell can take many forms, however, to keep it on topic a standard LIB will be used as an example, to introduce some of the reoccurring properties of batteries [12].

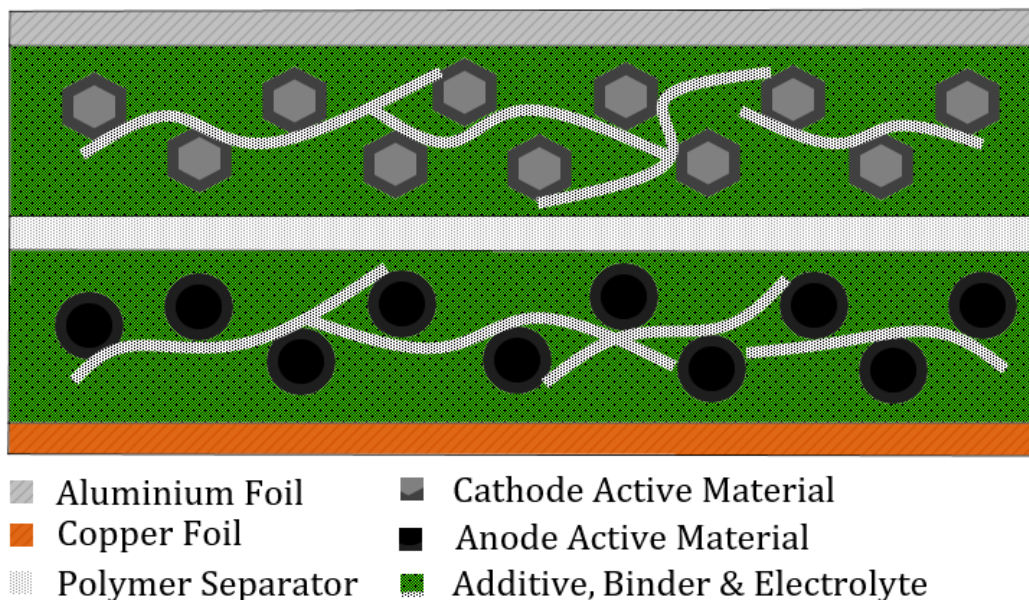


Figure 2.1: Diagram of the inside of a simple coin battery.

A coin battery is representative of the general galvanic cell, although all the components

behave differently from classic textbook examples using water soluble chemistries. The anode and cathode are separated into multiple components. The active material refers to the component that partakes in the electrochemical reaction. Graphite and Lithium Cobalt(III) Oxide (LiCoO_2) are the commonly used active materials in LIB used for portable electronic devices. The current collector acts as the substrate for active materials, while being able to conduct electrons with little resistance. Copper and Aluminum are the commonly used current collectors, as they resistant towards corrosion from graphite and LiCoO_2 respectively. The active materials are in a powder form, unlike the usual depictions in diagrams, and need additives to form a interconnected solid anode. The additives help with electrical conductivity and Li ion diffusion between particles. The mixture is made into a viscous slurry to create a homogeneous composition and to improve contact to the current collector. The most used additives are carbon powders to improve electron conductivity and polymer binders, such as polyvinylidene difluoride (PVDF) or sodium carboxymethyl cellulose (CMC) to create an network between the active material [12].

What is referred to as the electrolyte or solvent consists of a Li ion carrier, such as LiPF_6 for the electrolyte and additional organic solvents to improve the mobility of the ion carrier. The solvents used in commercial LIBs are dimethyl carbonate (DMC), diethyl carbonate DEC, ethyl methyl carbonate EMC, ethyl carbonate (EC) and propylene carbonate (PC). All of them are organic carbonates, also known as carbonate esters. The most important differences between the solvents is the dielectric constant, the melting point and the interaction with the electrodes. EC is used specifically because it more easily forms a stable SEI during the first charging cycle, while PC is avoided for graphite anodes, as it can diffuse between the graphene sheets and cause permanent damage. Combining multiple solvents can change the properties of the resulting mixture. A 1:1:1 ratio of EC, DMC and DEC is used in standard graphite based LIBs to improve the electrochemical stability and the lower the melting point of EC.

While the electrolyte is resistant towards redox reactions, it will still be reduced at the anode and oxidised at the cathode. When the electrolyte reacts with the electrons at the electrode surface they form a solid layer consisting of various Li containing products, such as Li_2O , Li_2CO_3 and LiOOCOR , where R depends on the solvent molecule that was reduced [13]. This layer is called the solid electrolyte interface (SEI). The disadvantage of SEI formation is the irreversibly loss Li ions, reducing the total capacity of the battery, and an increased impedance due to an additional transfer process across the SEI layer. The SEI is seen as an important component of a LIB, which acts as a protective layer, despite of the performance decrease. The electron conduction is poor within the SEI, which protects the electrolyte and solvent from further oxidation and reduction. The physical layer also prevents the electrolyte from inserting itself into the active material, which otherwise can cause irreversible damage to graphite electrodes [14].

The distance between the anode and cathode is shorter than usually depicted in diagrams. The closer to the electrodes can be packed together, the less space is wasted, increasing the energy density of the cell. The separator is a membrane used to prevent physical contact between the anode and cathode, while allowing the Li ions to pass through. The separator has a low electronic conductivity to prevent short-circuiting of the cell.

For a galvanic cell the distinction between anode and cathode is related to the movement

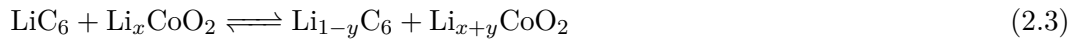
of electrons during discharge. The anode undergoes an oxidation reaction (eq. 2.1), which releases electrons that flow towards the cathode. Here the cathode is reduced by accepting the electron from the anode in a reduction reaction (eq. 2.2). For LIBs the Li ions act as the positive charge carrier that maintains charge conservation. The oxidation in the anode releases the Li cation. While the reduction in the cathode accepts a Li cation. For the standard graphite and LiCoO₂ cell the half-reactions are written as



for the anode and



for the cathode. We note that the reactions occur within crystalline materials, so the reaction is a gradual process that slowly changes the lithium content of the crystal, which makes



a more accurate depiction of what happens. This is especially the case for *LiCoO₂*, which requires Li atoms for the structural integrity of the crystal, setting the minimum value of $x \approx 0.4$ as the value of y slowly increases during discharge. Recharging reverses the reactions, resulting in the reversible reaction arrow in eq. (2.3).

2.2 Capacity and Stability

The capacity of an electrode determines how many Li ions can perform work via the electrochemical reaction. Since the relationship between Li ions and electrons in lithiation reaction is 1-to-1, the capacity is given in the unit [mAh/g], a derivative of [C/g], indicating the theoretical current the electrode can store in the form of charges. This capacity is also called the gravimetric capacity, as it is given per gram of active material. A high capacity does not only contribute to a higher energy density, it also indirectly leads to fewer charge-discharge cycles per unit of energy, which is beneficial for long term performance of the battery.

The theoretical capacity is based on a very simple assumption that the extend of the reaction between the Li ions and the active material is 100 percent. All the inserted Li ions will be stored during charging and are reversibly removed during the discharging process. The equation used for the theoretical capacity is

$$C = \frac{nF}{3.6M} \quad (2.4)$$

where n is the stoichiometric ratio between stored Li ions and atoms/molecules of the active material, F is Faraday's constant, M is the molar mass per atom/molecule of the active material, and 3.6 is a conversion factor from capacity in [C] to capacity in [mAh] [15].

Volumetric capacity is in the unit [mAh/L] derived by multiplying the gravimetric capacity by the density in [g/L] of the material. Gravimetric capacity is more important when considering material cost, while volumetric capacity is important when considering the portability of handheld devices and the size of battery packs in EVs.

There are multiple factors that decrease the capacity of an electrode as it is cycled. The reversibility of the electrochemical reactions, degradation of the active material, as well as the formation of the SEI, lead to a decrease in capacity. Formation of the SEI uses Li ions, preventing them from participating in the electrochemical reactions. Degradation of the anode creates grain boundaries, which decreases Li and electron mobility, and can promote formation of additional SEI between the grains. Irreversible reactions turn part of the active material into inert Li substances, which further reduces the number of Li ions that participate in the electrochemical reaction.

Capacity usually decreases with each cycle. While most of the SEI forms in the initial cycles, it can be damaged over time by strain or heat caused by the cycling process, which leads to additional Li ions being used to repair it. The active material will also degrade over time due to the diffusion processes and structural changes during cycling. The coulombic efficiency (CE) is used to describe the percentage of Li ions that have become inert during a single cycle. A relation that is used to highlight the importance of the CE is

$$Capacity(n) = Capacity(0) CE^n, \quad (2.5)$$

where n is the number of cycles and the CE is given as a decimal number. It describes that even a CE of 99.9% will still lead to capacity fade of 40% after 500 cycles. The relation does not hold for all electrodes, but is a reminder that what might seem as an acceptable CE for the first 50 or 100 cycles, will lead to long term capacity degradation. Drawing stronger currents also often leads to a lower CE and faster degradation [16].

2.2.0.1 Practical Capacity

The practical capacity is the actual capacity of the battery when not under standard temperature conditions or when the chemical equilibrium is disturbed. The charging and discharging process disturbs the equilibrium, as the reaction kinetics, diffusion processes, and electronic resistances, require time to change the concentrations to the new equilibrium. These effects are often lumped together as polarization, where the polarization increases with an increasing current density (More detail on this in section 2.3). This means that a higher current density will lead to a decrease in the practical capacity (competition between capacity and power density/charging time). Since most of limiting processes are Arrhenius dependent, an increase in temperature, will speed up these processes. This means that the practical capacity increases with increasing temperature, so long as it remains within a range that avoids thermal decomposition of the electrodes or electrolyte.

2.2.1 Electrode Potential and the Open Circuit Voltage

Electrical potential describes the potential energy of charged particles, similarly to how chemical potential describes the potential energy of molecules and materials. This means

that electrical potential is used to describe the differences in potential energy with regard to a chosen standard. Depending on the field of study the standard changes. The potential of the standard hydrogen electrode (SHE) is the usual standard for electrochemistry, although in the field of LIBs the standard is the reduction potential of Lithium metal.

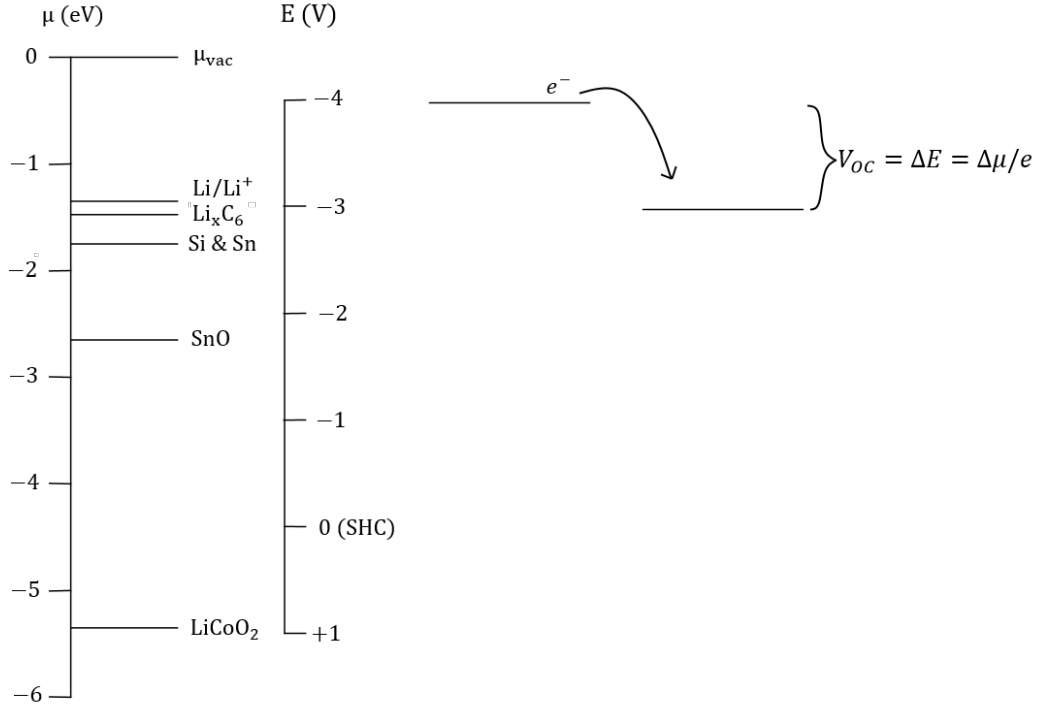


Figure 2.2: The scale of the electron chemical potential against the electrode potential

In solid state physics the potential energy of electrons in a material is described as the Fermi energy. The Fermi level is the chemical potential of the electrons in a given material, and describes the energy required to free the electrons from the material. The work function is the difference between the Fermi energy and the vacuum energy. In potential energy terms, the vacuum state is at 0 eV, since there are no electrostatic forces acting on the electrons in vacuum [17].

The relation between conventional current and the potential energy of electrons results in a flip of the scale, and the use of the SHE as the new standard means that 0V is not located at vacuum energy. Since the scale is the same, it allows for a very simple conversion between reduction potential E and the Fermi energy as seen in figure 2.2. This is why the difference in the Fermi energy or chemical potential are occasionally used to describe the open circuit voltage (OCV) of LIBs in the form of

$$V_{OC} = \frac{-\mu_c + \mu_a}{e} \quad (2.6)$$

where V_{OC} is the OCV, μ_i is the chemical potential of the anode a and cathode c , and e is the elementary charge. While the equation is too simplistic to give insight into the

more complex behaviour of electrodes during charging and discharging, it is able to help us understand what drives the movement of electrons between the two electrodes.

The reduction potential tells us the potential when comparing with other electrodes. For Lithium metal it is -3.05V , which means that a Li metal electrode attracts a strong conventional current. Electrode potential describes where conventional currents flow towards. Li metal has the lowest value of any electrode, making it the deepest point on the potential scale. Just like water flowing downhill, so will conventional current flow to the lowest potential.

Physically it means that Li metal oxidises easily, as it wants to be release the electrons. The work function can help with understanding this. A low electrode potential result in a Fermi energy closest to the vacuum energy. This means that the electrons are easily removed from Li metal, and oxidation reactions are more favourable when compared to other materials. When the reaction happens the metal turns into Li ions and free electrons, although this requires an oxidant to be present. The violent reactions between Li metal and air or water are examples of how easily the in Li metal electrons are transferred.

2.2.2 Thermodynamics and the Nernst Equation

The OCV and the cell potential that is described by the Nernst equation are the same value. The Nernst equation can be derived in multiple ways, however, a simple version is the thermodynamic argument. We first make the assumption that the reaction is reversible, and that the work consists of two terms. The first is expansion work (related to pressure and volume) and the second is non-expansion work ϕ (all other types of work)

$$\delta q = TdS, \quad \delta w = -pdV + \phi. \quad (2.7)$$

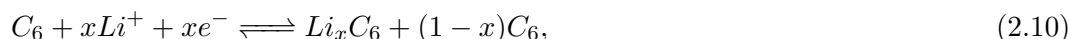
The change in internal energy is equal to the change in work and change in heat, where we have expansion work and non-expansion work ϕ

$$dU = \delta q + \delta w \iff \phi = dU - TdS + pdV \quad (2.8)$$

where the relation between enthalpy and internal energy is given as $dH = dU + pdV$. Substituting this into 2.8 and comparing it to the Gibbs energy $dG = dH - TdS$ gives us

$$\phi = dG = dH - TdS \quad (2.9)$$

therefore the Gibbs energy is a measure of the maximum non-expansion work a chemical reaction can perform per mole. We take this non-expansion work to be the electrical work. For the intercalation of Li ions in graphite we can take the earlier reaction (eq. (2.3)) and include the extend of the reaction x ,



where a greater extend of the reaction is related to the non-expansion work through the Gibbs energy,

$$\phi = dG = \Delta_r G dx, \quad (2.11)$$

therefore the Gibbs energy is a measure of the maximum non-expansion work a chemical reaction can perform per mole. We take this non-expansion work to be the electrical work. For the intercalation of Li ions in graphite we can take the earlier reaction

$$dq = -neN_A dx = -nF dx. \quad (2.12)$$

To recover the work we take the relation between electrical work and the electrical potential

$$\phi = Edq = -nFEdx, \quad (2.13)$$

which gives us the Nernst equation after equating the two forms of work

$$\Delta_r G dx = -nFEdx \iff E = -\frac{\Delta_r G}{nF}. \quad (2.14)$$

The Nernst equation is then naturally expanded by including the law of mass action from the Gibbs energy,

$$E = -\frac{\Delta_r G^\ominus}{nF} - \frac{RT}{nF} \ln \frac{\prod a_{products}}{\prod a_{reactants}} \quad (2.15)$$

Note that an assumption of the reaction being completely reversible is not true, and some is lost to entropy. These losses are multiple orders of magnitude smaller than the useful work extracted from the reaction, which makes the assumption fair.

2.2.2.1 Deviation from Ideal Conditions

The limitations come from the assumptions made in the Nernst equation. LIBs do not work under ideal conditions. The Li ions are dissolved in the solid phase of the anode, and not in an aqueous solution. Using fully intercalated LiC₆ as an example we get a Li ion concentration of

$$c_{Li^+} = \frac{C_{anode} \rho_{anode}}{F}, \quad (2.16)$$

which for a graphite anode results in a concentration of 27.8 mol/L when fully lithiated. Assuming a linear relation, even when the extent of reaction is low, the concentration would deviate from the ideal condition.

The observed relation between the electrode potential and the Li content is a strong decrease in potential when the material goes from 0% Li content to the 10-20% Li content. The drop in potential differs based on the anode, however, even the anodes with smaller drops still experience a change in potential of approx. 0.5V. A value that is fairly substantial when compared to the nominal voltage of LIBs at 3.6V. The difference in the electrode potential based on the ideal conditions of the Nernst equation is 0.025V (at 298K) when comparing 0% and 100% Li content.

The most common explanation is that small amounts of Li metal start to form on surface of the active material, causing the potential to drop towards the Li electrode potential. Faster charging rates have been linked to steeper declines in electrode potential, as higher concentrations of Li ions create better conditions for Li plating [18]. Most of the plating will dissolve and become intercalated as Li ions, but can still lead to some decrease in CE, depending on how much remains.

2.2.3 Structural Evolution

The value and shape of the voltage curve in relation to the SOC depends on the structural changes that occur during the discharge process. The usual assumption is that the standard electrode potential remains constant, however, structural changes occur during lithiation, which influence the chemical potential of the electrode, and thereby also change the standard electrode potential. How this change influences the electrode potential as a function of the extend of the reaction x , we can take equation 2.14 and instead rearrange it as a gradient

$$E(x) = -\frac{1}{nF} \frac{d(\Delta_r G)}{dx}, \quad (2.17)$$

which means that a linear change in the change of Gibbs energy results in a constant potential curve in relation to the extend of the reaction. This is particularly of interest due to the importance of the shape of the potential curve. A flat potential curves is preferred to maintain a stable potential to avoid changes in the OCV as the SOC decreases.

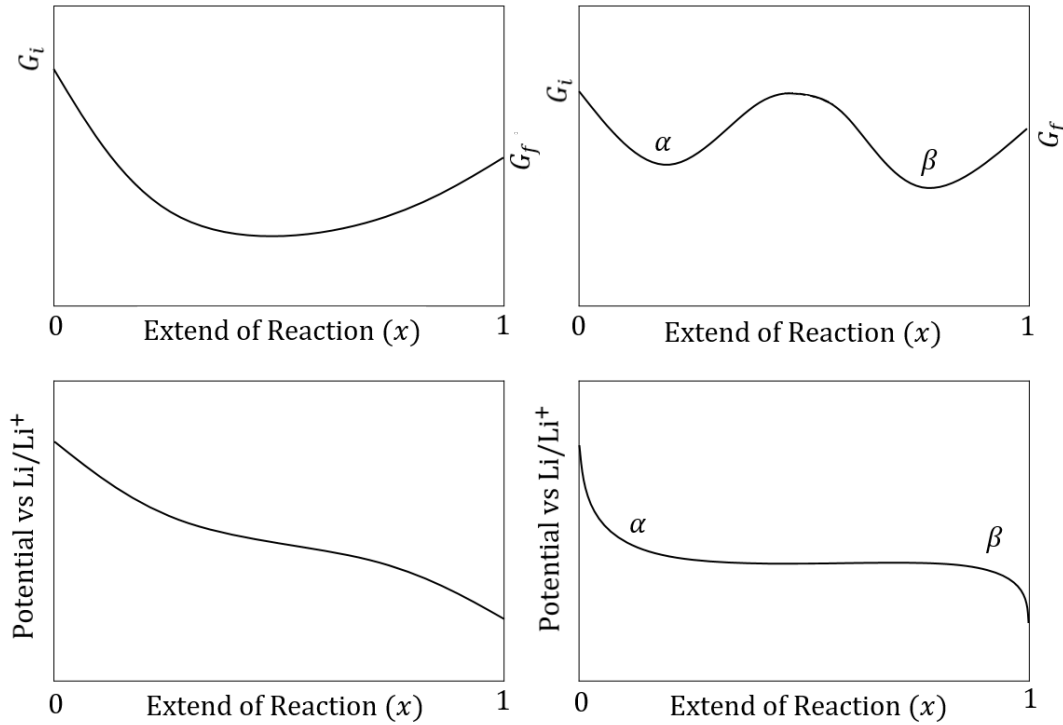


Figure 2.3: Depicting the different voltage profiles as a result from phase changes during the lithiation process.

Whether the change in Gibbs energy is linear depends on the number of phases that coexist during the lithiation process. The Gibbs energy of mixing can help to illustrate this. Miscible phases have a low excess enthalpy when forming a solid solution, and immiscible phases have a high excess enthalpy. The mixing entropy is the same for any system regardless of the excess enthalpy. For a binary system the extend of reaction can be used to describe the change in Gibbs energy from mixing as

$$\Delta G_{mix} = nRT[x \ln x + (1 - x) \ln 1 - x] + nR\xi x(1 - x) \quad (2.18)$$

and for the total change in Gibbs energy for the initial and final phase

$$\Delta_r G = xG_f^\ominus - (1-x)G_i^\ominus + \Delta G_{mix}. \quad (2.19)$$

The value of ξ depends on excess enthalpy, where positive values increase the total Gibbs energy, and describe the immiscible case.

Figure 2.4 shows two different curves for the absolute Gibbs energy. (a) corresponds to low excess enthalpy resulting in ideal mixing, while (b) corresponds to high excess enthalpy resulting in formation of at least two phases. The two valleys depicted in (b) convey that it is more favourable to form a phase with low Li content (β) and a phase with high Li content (α). The Gibbs phase rule tells us that the degrees of freedom are related to the number of components and phases

$$f = (2 + c - p) - 2 = 2 - p, \quad (2.20)$$

where $c = 2$ corresponding to the lithiated and delithiated state. Temperature and pressure are considered constant inside a battery, reducing the degrees of freedom by 2. The resulting equation 2.20 will tell us the degrees of freedom for the miscible and immiscible cases.

The ideal mixing case has the lithiated and delithiated components in a single phase, resulting in a degree of freedom of 1. This means that the variable extend of reaction (Li content) can be changed freely without a phase transition. The resulting electrode potential depicted as (c) will follow a gentle sloping curve as the lithium content increases.

The coexistence of two phases reduces the degrees of freedom to 0. This means that changes in the extend of the reaction cause a phase transition. In this case α converting into β as the Li content increases. If the system is in equilibrium, the phase transition occurs when the chemical potential of both phases is equal. Similar to melting or evaporation, applying the Gibbs-Duhem equation 2.21 at constant volume and pressure, means that the Gibbs energy is constant during this first order transition and the change in Gibbs energy is zero until all of phase α has transitioned into phase β .

$$G = \mu_\alpha N_\alpha + \mu_\beta N_\beta = \text{constant}; \quad dG = \mu_\alpha dN_\alpha + \mu_\beta dN_\beta = 0 \quad (2.21)$$

From the earlier description of the Nernst equation (eq. 2.14), the electrode potential remains constant, so long as the phase transition occurs. This results in a plateau in the potential profile, which is also called an L-shaped curve [19]. Note that this only applies to the shape of the curve, and the Gibbs energy in the ideal mixing and the phase separation scenario start and end at the same values.

2.2.4 Nano Sized Effects

The properties of the bulk material and a single atom are different. Nanoparticles bridge the gap between the two as the properties approach that of the bulk material as the size of the nanoparticles increases. This also affects the electrochemical properties of active materials, if they are synthesised as nanoparticles [20].

The thermodynamics of particle formation are favourable for bonding between atoms, which means that atoms aggregating into a larger volume is energetically favourable.

Atoms at the surface have fewer bonds making it less energetically favourable and is the reason for the energy cost related to a larger surface area. As the particles decrease in size, the relative number of atoms at the surface increases, which increases the Gibbs energy. This results in a decrease (more negative) electrode potential [21, 22].

2.2.5 Summary

The potential plays a central role in the performance and stability of a cell. As mentioned in chapter 1 there is a conflict between higher power output and the safety and lifetime of a cell. Lower anode potentials are desired to increase the power density, but the other components restrict this. The potential of the anode has to be aligned with the other components of the battery. The current collector and the solvent used for the electrolyte are both directly in contact with the anode. If the electrode potential of the anode is lower than the reduction potential of the electrolyte, solvent and copper foil, it would result in side reactions that would lead to permanent damage of the cell. A higher electrode potential decreases the driving force behind the electrochemical reaction, however, can also improve the safety of the anode. Lithium metal plating occurs if the electrode potential is close to the Li^+/Li reduction potential. If the anode experiences kinetic issues, a build-up of Li ions can shift the potential below the plating potential, and the result is the formation of Lithium metal on the anode surface. Aside from absolute values the preferred shape of the voltage profile is the L-shape, since it gives a more consistent energy output during the entire discharge. This will also depend on the corresponding voltage profile of the cathode that is used, where currently used cathodes exhibit a L-shaped profile.

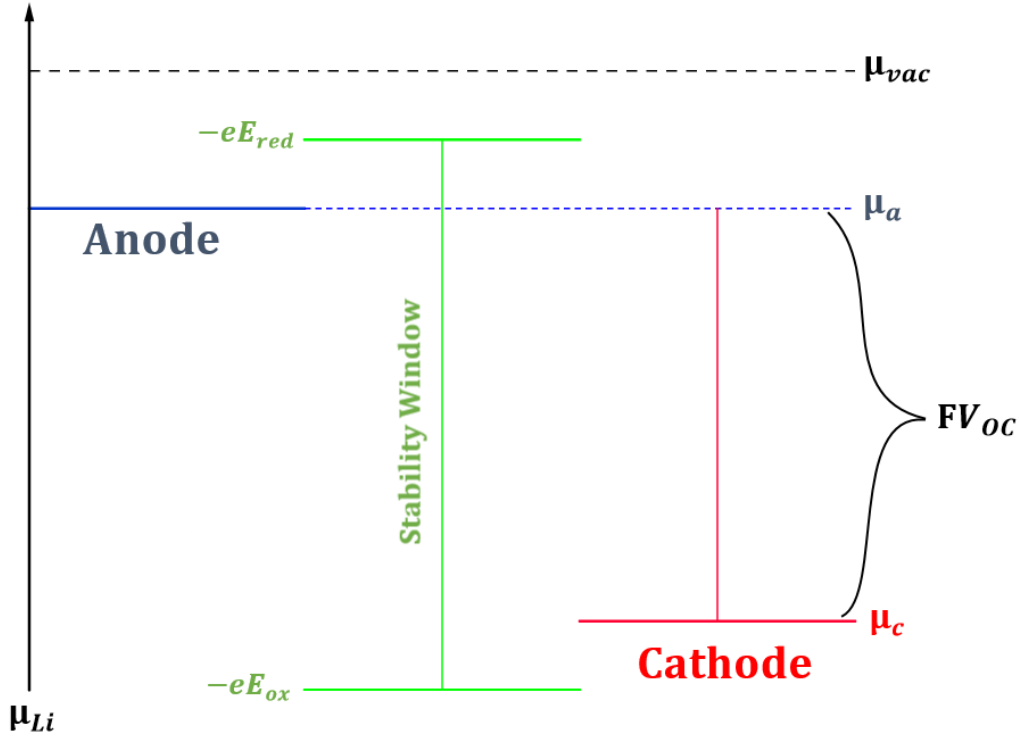


Figure 2.4: The OCV is given by the difference between the anode and cathode, however, is limited by the voltage window of the electrolyte.

2.3 Polarization and the Closed Circuit Voltage

The OCV only applies during equilibrium, and the changes in potential mentioned so far, have no relation to the active processes that occur during the non-equilibrium state of the battery. During charging and discharge, a current flows through the battery, causing a movement of electrons and Li ions. The corresponding potential difference is the closed circuit voltage (CCV), a term used to describe a completed circuit where current can flow. The dynamics of the charge carriers as well as the kinetics of the Li storing reactions force the battery out of equilibrium. How the various types of processes relate directly to impedance will be described in section 5.2. For now these processes can be considered as multiple types of resistances that reduce the working potential during discharge, and increase the applied potential during charging, always decreasing the CE of the battery. These resistances are often broadly called over-potential or polarization and relate to the OCV and CCV as

$$V_{CC} = V_{OC} \pm \eta, \quad (2.22)$$

where V_{CC} is the closed circuit voltage (also called the working voltage) and η is the over-potential. The sign of the over-potential changes to increase the CCV during charging and decrease the CCV during discharging. This hysteresis of the voltage profile remains even at very low currents, and is most likely caused by polarization effects that are inherent to the material. These include reordering of bonds and phase transitions, which require an activation energy, but are not directly related to the lithiation or delithiation [23].

Ohmic polarization is related to the Ohmic resistance experienced by the electrons and the Li ions. The resistance experienced by electrons can describe the over-potential as a gradient dependent on the thickness of the electrode

$$\frac{dV}{dx} = \frac{I}{\sigma A}, \quad (2.23)$$

where σ is the electron conductivity of the material, A is the cross sectional area of the electrode, I is the current, dx is the infinitesimal distance the current has to travel, and dV is the infinitesimal drop in potential as a result of the flowing current. Writing it this way highlights that the Ohmic resistance experienced is not the same for all the charge carriers. It also describes that all the components should be as thin as possible to decrease the distance the charge carriers have to travel. Li ion resistance uses the same formula, with the electron conductivity replaced by the ionic conductivity. A consequence of the resistance is that the lithiation process is favoured at the locations where the combined electron and ionic resistance are lowest. These regions would be the close to the separator and current collector if the electrodes are too thick.

The conductivity of Li ions is a case of ionic impurities moving through a solid electrode or a liquid electrolyte. The Nernst-Einstein equation describes the ideal situation where the concentration of ionic impurities is small, and requires additional constants to account for the high concentration of Li ions.

$$\sigma = \frac{z_i c_i F^2 D}{H_R RT}, \quad (2.24)$$

The Haven ratio describes the relation between self-diffusion (also known as tracer diffusion) and the ionic conductivity of a specific ion in a specific material and is measured empirically. The ratio is usually between 0.1 and 1, where 1 is the ideal case and there is no difference between ionic conductivity and self-diffusion.

Charge transfer polarization is related to process of Li ions diffusing from the electrolyte to the electrode crossing the electric double layer. This step is the lithiation and delithiation process, where further diffusion inside the electrode causes the growth of the lithiated or delithiated phase. The Butler-Volmer equation describes this process similar to reaction kinetics

$$j = j_0 \left[\exp \frac{\alpha_a n F \eta}{RT} - \exp \frac{-\alpha_c n F \eta}{RT} \right] \quad (2.25)$$

where j_0 is the drawn or applied current density, j is the actual current density, α is the dimensionless charge transfer coefficient describing the favourable transfer direction, and η is the same over-potential as earlier. There is a continuous back and forth transfer of ions with the net transfer depending on the CCV (expressed through the over-potential). The polarity of the potential decides the direction of the transfer. A lower over-potential results in a higher current, as the over-potential acts like an activation energy for the electrical transfer process. Since the Butler-Volmer equation describes the current density, it follows that a greater surface area of the active material will result in a greater current, and faster lithiation and delithiation. For ideal cases where the applied voltage is small and the resulting over-potential is also small, eq. 2.25 can be simplified using $e^x \approx 1 + x$ and rewritten to reflect the charge transfer resistance

$$R_{CT} = \frac{RT}{FAj}, \quad (2.26)$$

where the area A has been added to reflect the resistance of the entire electrode. The important thing to note is that the resistance is inverse proportional to the actual current density j and the surface area of the electrode.

Concentration polarization is when the Li ion concentration is not uniform throughout the battery. During discharge it would mean that the charge transfer process in the anode releases Li ions faster than they can diffuse away. From a kinetic perspective, the diffusion becomes the rate limiting process. For the cathode that would mean that, the Li ion concentration will decrease, as the Li ions are transferred faster than they can be supplied. The result is a high concentration of Li ions at the anode, a low concentration at the cathode, and the formation of a Li ion concentration gradient across the double-layer that creates a chemical driving force in the opposite direction of the discharge reaction, resulting in a decrease of CE and practical capacity. The same gradient does also increase the diffusion from the anode to the cathode, however not enough to prevent concentration polarisation [24].

Concentration polarization can be observed when the current is increased to a point where the practical capacity of a cell decreases significantly more than what is expected from the linear polarization drop from Ohms law. When Li ion diffusion is the limiting factor, the increased current goes to waste, as the additional charges are dissipated through wasteful processes unrelated to lithiation or delithiation. Sometimes these processes are harmful for the anode, which is why the CE is lower and the lifetime capacity decreases faster at higher currents. Concentration polarization is managed by designing a battery where the diffusion processes are able to transport ions to match the lithiation and delithiation reaction rates. Modelling of LIBs is done by calculating characteristic times for each of these processes [24, 25].

The porosity can be adjusted through compression of the anode material. The performance in relation to the porosity depends on pathway the Li ions and electrons can travel throughout the electrode. High porosity increases the surface area of the active material and also allow the electrolyte to penetrate the electrode, which increases the contact area between electrolyte and active material. This can be beneficial, since it decreases charge transfer resistance and increases the rate of Li ion transfer from the electrolyte to the active material. Downsides are related to the distance electrons have to travel, as higher porosity usually means a less direct pathway throughout the electrode. While electron conductivity is usually higher than the Li ion conductivity, this can still lead to concentration polarisation if the dimensions of the anode are not optimised for the increased transfer rate between the electrolyte and the active material. An increase in the surface area between the anode and the electrolyte also allows for more SEI growth, which will decrease the initial CE of the cell.

2.3.1 Summary

No matter how high the OCV is, the power output of a battery requires current. Increasing the current for a greater power has the unfortunate side effect of decreasing the potential and the practical capacity as a side effect of the various polarisation processes. These issues can be alleviated by optimising the dimensions of the electrodes and separator to match the characteristic times of the polarisation processes. Diffusion of Li ions in the

electrolyte and anode composite is improved by using thin anodes that have a large surface area. Active materials with a small particle size improves the diffusion in the solid-state. Smaller particles would mean less active material, however, studies have shown that this is offset by the a decrease in polarisation, resulting in similar practical capacities [24].

Using binders and additives, while not the primary active material, do not decrease the practical capacity significantly, and can be used to enhance the other properties of the anode, such as stability, conductivity, and interconnectivity of the active material particles [26].

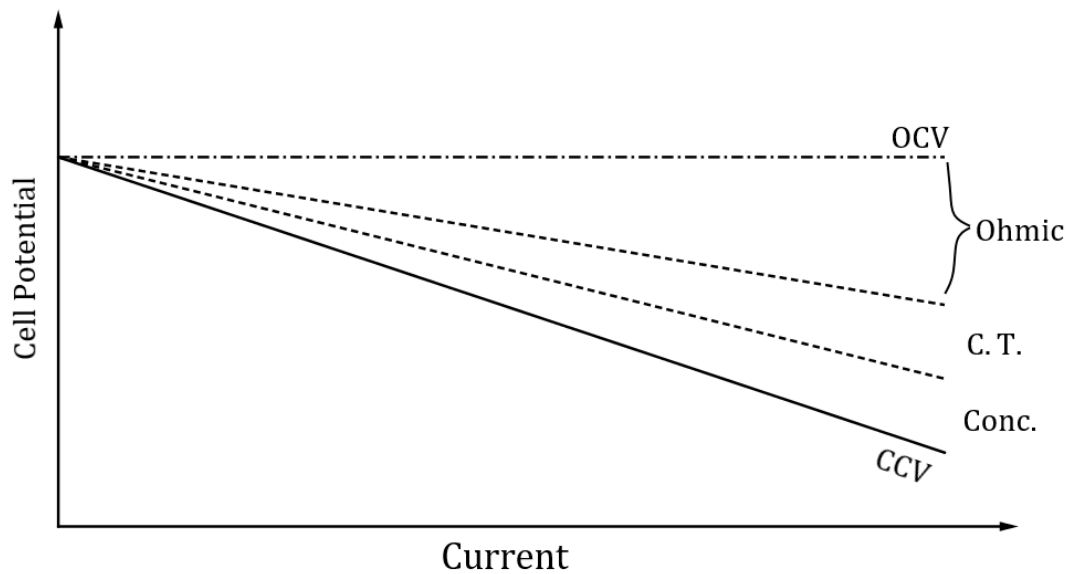


Figure 2.5: Different contributions to the polarization, causing a drop in the working voltage as the current is increased.

Anode Development 3

Chapter 2 described the performance of electrodes and batteries in general and this chapter will focus on anodes specifically. The reason is that there is no real expectation that ZIFs have good performance as cathodes. Cathodes are materials that store Li ions at a high potential, which is far less common than materials that store Li ions at a low potential. The potential of any material decreases when Li becomes part of the structure bringing the potential closer to the value of Li metal (examples of this will be given in this chapter). Following the logic from section 2.2.1 a good cathode strongly binds the electrons during discharge, and requires a strong applied potential to remove the electrons during charging. The most common cathode, Li_xCoO_2 , utilises the reduction of the $\text{Co}^{3+}/\text{Co}^{4+}$ redox pair, which is a process that occurs at a high potential (not to be confused with an energetic process) [27]. It is a rare transition only found in a few materials due to how unstable the ions are compared to Co^{2+} . The material selection is further limited by the types of counter ions that can be used. Oxygen or oxygen containing poly-anions are the best candidates due to their strong electron affinity, which allows the formation of stable bonds with the high oxidation state transition metals without being oxidised. Commercial cathodes have practical capacities in the 120-180 mAh/g range, which is considered low when compared to anodes. Finding cathode materials with a high electrode potential that also have good cycling stability and capacity is difficult due to the specific electrochemical requirements [28].

It is more likely that ZIFs can be used as anode materials, based on chemical composition and the lithiation processes that occur in anodes. This section will be a review of the various anodes that have been used and are currently in consideration, with the purpose of understanding desirable and undesirable properties of anode active materials. As well as using that knowledge to understand the lithiation process in ZIFs. The intercalation, alloying and conversion reactions will be explored, and their relation to the previous battery properties will be considered.

3.1 Lithium Metal Anodes

Lithium metal anodes were the first type of anodes used in research regarding lithium based batteries. The energy density of Lithium was already well understood from its physical and thermodynamic properties, however, there were no good cathodes and electrolytes to facilitate it. It was the discovery of sulphide cathodes capable of storing Li ions together with electrochemically stable organic solvents (EC, that made it possible to create the first battery using Li ions as charge carriers.

A pure lithium metal anode still has the highest energy density of any anode type. This is

because it is the direct source of the charge carriers, meaning that it no form of alloying, conversion or intercalation takes place. The ions are directly deposited on the anode surface and all the mass of the anode goes towards the capacity of the battery. Metallic bonding also allows for a denser packing than alternative anodes that are made from covalent structures.

Among the metals Lithium also the lowest electrode potential at $-3.05V$, giving it great values for the OCV. It has the lowest density of any metal at 0.535 g/cc , which usually would be a drawback, however, since all of the mass goes towards the capacity, it still has highest volumetric capacity. It has a theoretical capacity of 3800 mAh/g , which is lower than some other metals, but this is also the value of the practical capacity, which is not the case for other anodes.

The problem with Lithium metal as the anode for a rechargeable battery is the formation of dendrites caused by the uneven deposition of Li ions during the reduction onto the metal surface. These dendrites can puncture the cell or cause a short circuit, depending on the direction of the dendrite growth. The low melting point of Li metal (180 Celsius) can also result in melting of the anode if the cell has poor heat dissipation.

While lithium metal anodes have safety issues when used as rechargeable battery, it showed that the performance of the new materials and of Li ions as charge carriers, far succeeded that of earlier batteries. The small size of the Li ions (76 pm) relative to its closest competitor the sodium ion (102 pm) [29], results in better diffusion through the electrode materials and has a greater energy density. The lower weight of a single Li ion, also means that the charge per mass is greater compared to other ions. The performance of LMBs is so good that they are still used for primary batteries (single use) and there is still active research in trying to stabilise the anode for secondary batteries. Especially the all-solid state batteries are gaining interest, as the solid electrolyte does not allow for same dendrite growth, making Li metal a good candidate for the anode.

3.2 Graphite Anodes

LIBs function differently from LMBs. The anode is no longer the source of the Li ions, a change made possible by using metal oxide cathode with pre-inserted Lithium. Graphite takes the role of storing the Li ions once the battery is charged. Intercalation is the mechanism of storage and behaves more as an insertion of the ions, rather than forming a full covalent bond.

Graphite was the first commercially used anode for the use of LIBs. It has a far lower theoretical capacity than Li metal at 372 mAh/g with a practical capacity for high-quality graphite at 360 mAh/g . This trade-off in capacity was made for long-term safety and stability of the battery. Carbon is also a very abundant element, making it easier to produce graphite, although high quality graphite can be expensive. The overall Li content in each battery is also lower, since the anode no longer consists of a pure Li anode.

Graphite consists of graphene sheets, which are a 2D plane of carbon atoms configured in a honeycomb pattern. Graphite stacks these sheets in an ABAB or ABCAB stacking pattern. Defects in graphite can disrupt the stacking, which creates amorphous regions,

or holes in the sheets. All of these defects reduce the total number of sites where Li can be stored, leading to a reduced capacity. These defects are the cause of the practical capacity being lower than the theoretical capacity.

The intercalation reaction of Li ions into graphite works by intermolecular interactions between the conjugated graphene sheets and the Li ions. No covalent bonds form, so the structure of the graphite remains mostly the same. The only structural change that occurs is that the packing changes with each layer that forms from the intercalated Li ions. When the maximum capacity has been reached, the packing has changed into AAA stacking for the alternating bilayer structure of graphene sheets and Li ions.

The reaction formula of the intercalation is repeated from earlier,



where it is certain that the Li ions are stored, and that the electrons have contributed to charge conservation. The oxidation state is not entirely certain, however, the Li still has a partial ionic character after intercalation, indicating a partial transfer of electron density from the graphene layers to the Li ions [30]. The graphene sheets are able to accept electrons from the external circuit into the π band, a band constructed from the overlap of the $2p_z$ orbitals of each carbon atom. The spatial direction of the $2p_z$ orbitals creates a quadrupole with the negative ends pointing perpendicular to the plane, resulting in the attractive cation-quadrupole interaction that is present in any aromatic ring structure [31]. This interaction is strong enough to align the Li ions with the center of the hexagonal rings, while also limiting the intercalation limit to the number of quadrupole sites resulting in the 1:6 ratio [32].

The potential profile of Li_xC_6 is closely related to the structural evolution and the content of Li ions (x), which makes graphite anodes a good example to describe some of the phenomena. The insertion of Li ions is split into different stages, all corresponding to changes in the potential profile. At a low content of Li ions ($x < 0.2$) the electrode potential is approx. 1V vs Li. This is the first stage (IV), where all layers have a low concentration of Li ions. This potential drops quickly to approx. 0.25V at $x = 0.2$ as the concentration of Li ions increases. The exact reason for the steep drop has been attributed to small amounts of Li metal plating as the Li ions diffuse into the graphite [18]. Li ions start to intercalate in the layers that already have the highest concentration of Li ions, filling the layers unequally, resulting in different stages of intercalation. When a layer is fully intercalated, the packing of layers changes, creating distinct phases. The existence of multiple phases leads to the observed voltage plateaus as the transition between phases occurs (as explained in section 2.2.3). The difference in the phases is not large, resulting in only small steps in the voltage as the phase transition is completed. Completion of each stage is shown in fig. (3.1). The final potential is approx. 0.1V vs Li at $x = 1$ when all the layers have changed to AAA packing [30].

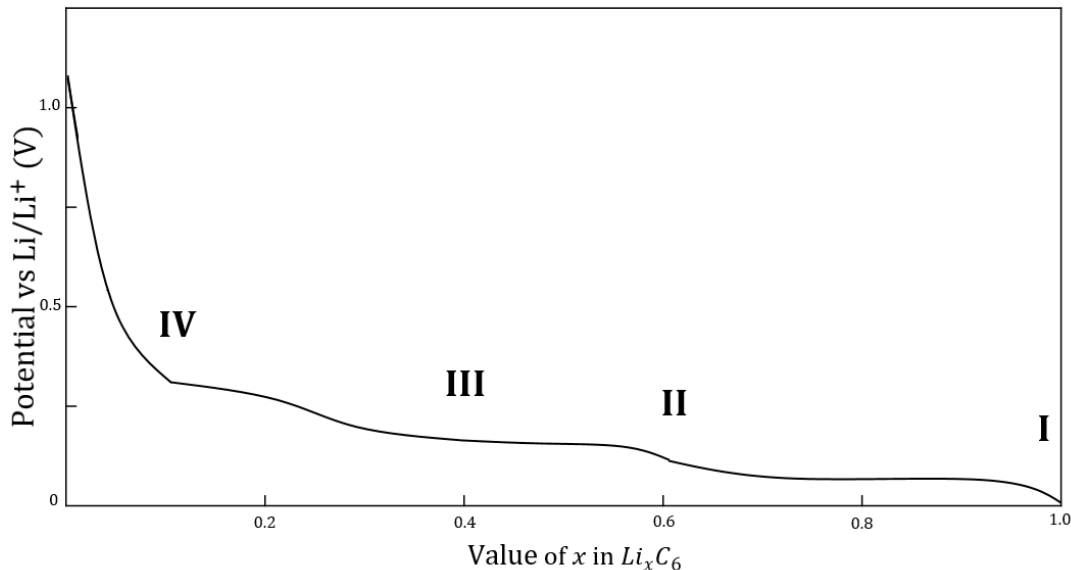


Figure 3.1: Sketch of a the potential curve for the graphite anode. The roman numerals indicate the different stages of intercalation.

The intercalation reaction has a good voltage profile due to the potential slope having multiple plateaus at low potential values. Lithium plating can become an issue due to a fairly low rate of intercalation and an electrode potential close to that of the Li reduction potential [33]. Both events lead to a reduction of the capacity, and excessive SEI formation can further increase the probability of Lithium plating due to decreased diffusion of Li ions [34]. While LIBs made with graphite are far safer than LMBs, the Li plating and dendrite formation does still cause enough issues to make news headlines regarding exploding batteries or burning EVs [35]. Since these safety concerns are related to the lithiation rate of graphite, it gives another reason to improve the performance of anodes.

3.3 Metal Alloying Anodes

The group IV (group 14) metals were some of the first up for consideration as anode materials to replace graphite, due to their high theoretical capacities [1]. They have a far greater theoretical capacity than graphite due to the alloying reaction, which can bind more Li ions than the intercalation process in graphite. Silicon (Si), tin (Sn), germanium and lead fall into this group. Si has garnered the most attention, due to the non-toxicity and abundance of the metal. Sn is far less abundant, but still studied due to the similarities between the two metals [36]. The postulated composition of the lithiated alloy is Li_{22}M_5 , based on the crystal structures of other known alloys [23]. This gives the alloy a stoichiometric ratio of 4.4:1, meaning that it is able to store 26.4 times more Li ions per mole than graphite. Si has a theoretical capacity of 4200 mAh/g and Sn the theoretical capacity of 790 mAh/g. The actual observed composition for Si is $\text{Li}_{15}\text{Si}_4$ with a theoretical capacity of 3580 mAh/g. Si becomes amorphous during the lithiation and crystallises into $\text{Li}_{15}\text{Si}_4$ at a high concentration of Li. The Sn alloying goes through

multiple crystalline phases and does end up as the predicted $\text{Li}_{22}\text{Sn}_5$ crystal phase when fully lithiated [23].

The alloying process, unlike the deposition on Li metal anodes, requires diffusion of the Li ions to fully lithiate the metal particles. When the Li ions are reduced they coordinate with the Si or Sn forming an alloy,



The closer packing of atoms also means that the distance the Li ions have to travel within the active material is shorter, ideally leading to faster lithiation and delithiation processes than in graphite anodes.

The potential profile of Si starts at 1V vs Li, and reaches a plateau of 0.5V during a two-phase equilibrium of amorphous Li_xSi and the final crystalline $\text{Li}_{14}\text{Si}_4$ phase [23]. The fully lithiated crystal has a potential of 50mV vs Li. The average potential is usually considered to be approx. 0.4V vs Li. It is speculated that the sudden crystallization from the amorphous phase is related to the high Li mobility in the alloy, which allows for an easy rearrangement into the crystalline structure. During delithiation the alloy will become and remain amorphous, even if the initial Si used was crystalline [23, 36]. The potential profile of Sn is similar to Si, with the exception of multiple plateaus, due to the many phase transitions during the lithiation process [36]. All the plateaus are in the potential range between 0.7V and 0.4V, decreasing with increasing Li content. The average potential is approx. 0.5V [23, 36].

Metal based active materials are already tightly packed, which means that the alloying process results in an expansion to make space for the Li ions. The values for the volume expansion vary, with conservative estimates claiming a volume expansion of 280% for Si and 240% for Sn [36]. Volume expansion causes multiple issues. Pulverization is caused by the formation of cracks in the active particles during expansion. A decreased contact with the current collector is caused by the strain of the continuous changes in volume during cycling. Additional SEI forms when the cracks form or when part of the old SEI is destroyed during cycling. The three mentioned events create new surfaces where electrolyte can be reduced to become additional unwanted SEI. The formation requires Li ions, which decreases the capacity. The newly formed SEI creates regions within the anode with low electron conductivity. In the worst case it can isolate some of the active material, preventing it from contributing to the electrochemical reaction (fig. (3.2)) [12, 36, 37]. These issues result in a poor CE as the anode becomes more damaged with each cycle. In the worst case a complete loss of contact with the current collector will cause a complete failure of the battery [12].

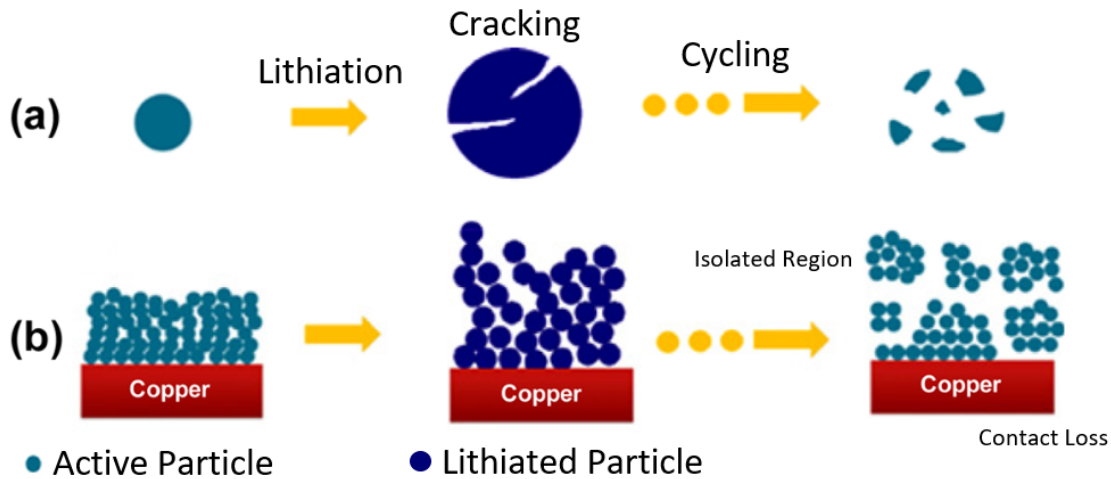


Figure 3.2: (a) Crack formation during a single cycle leading to the pulverisation of the active material after multiple cycles. (b) Reduced contact with the current collector, formation of isolated regions, and additional space for SEI formation after repeated cycling. Modified figure from ref.[37]

Aside from the pulverisation, alloying has issues with the reversibility of the electrochemical reaction. Part of the Li remains as the alloy when the battery is discharged, resulting in a poor CE during the first cycle, and a permanent loss of capacity. Attempts to alleviate the issues with alloying type anodes are often related to forming various nano-structures [23, 36]. As mentioned in section 2.2.4 and 2.3.1 smaller particles can improve the performance, even when using less active material. The reversibility is improved due to a combination of a slightly lowered electrode potential and shorter diffusion times. Smaller particle size also increases the free volume of the anode, increasing the space in which the particles can expand into. Particle sizes below 150 nm were sufficient to prevent pulverisation of the active material [38]. Using amorphous Si or Sn also decreases the total volume expansion, since the amorphous already has a larger volume than the crystalline counterparts, although this does decrease the volumetric capacity slightly [23]. A drawback of smaller particles is that there is more surface for the SEI to grow onto. Various coatings and binders are used to help decrease the growth of the SEI while also absorbing the stress from the volume expansion. Coatings can decrease the diffusion of Li ions, slowing down the volume expansion, and allowing for a more even growth, decreasing the strain. Using binders can help absorb some of the stress, while increasing the integrity of the anode as a whole [12]. Si being a semi-conductor also has a lower electron conductivity than both graphite and Sn. The smaller particle size together with coatings and binders also improve the overall conductivity of the anode.

3.4 Conversion

Conversion active materials is a very broad category as it consists of any mineral that has an electronegative atom capable of binding Li ions. The conversion reaction differs from alloying, as it does not form any alloy. Instead, the electronegative anion interacts with the Li ions, and the electropositive metal cation is reduced and separates. The exchange of the anion between the metal cation and the Li ion causes significant changes

in the structure of the active material. The structural changes upon conversion cause the formation of a composite made of metal nanoparticles embedded in amorphous Lithium compounds (usually Li_2O).

The ratio of metal to oxygen is not important to the reaction itself, so long as it contains oxygen (or another non-metal cation) and metal cation that form a stable crystal. The conversion reaction can be written as



where the stoichiometric ratio between Li and O is 2:1, as per their respective standard oxidation state of +I and -II. The metal M is usually a transition metal, with some common examples being iron, manganese, cobalt and nickel.

The electrode potential depends primarily on the anion. Sulphur and oxygen are the commonly used anions. Oxygen is the stronger oxidiser, due to the difference in the electron affinity of the 2p valence orbital, compared to the 3p valence orbital in Sulphur. The oxygen creates a stronger bond, which requires more energy to break during the formation of Li_2O resulting in a lower electrode potential. Therefore metal oxides have lower electrode potential and are therefore more commonly used for conversion anodes. Despite this, the potential profile is not as favourable as that of the previously mentioned anode materials. The average electrode potential is higher at 0.8-1.1V, and there is no plateau, resulting in a steadily decreasing power output, rather than the preferred stable power output.

The volume expansion is usually lower than that of alloying type anodes, however the separation process of the metal particles can lead to additional issues such as leaking material into the electrolyte and aggregation of the active particles. The requirement to reverse the separation process also decreases the reversibility of the electrochemical reaction compared to alloying and intercalation anodes. The metal particles that form are regions with poor Li ion conductivity, while the Li_2O regions have poor electron conductivity. The combined effects of the poor diffusion, poor conduction and the separation process, result in worse reaction kinetics than alloying type anodes [39]. This is reflected in the capacity of conversion active materials. The reversible capacity lies between

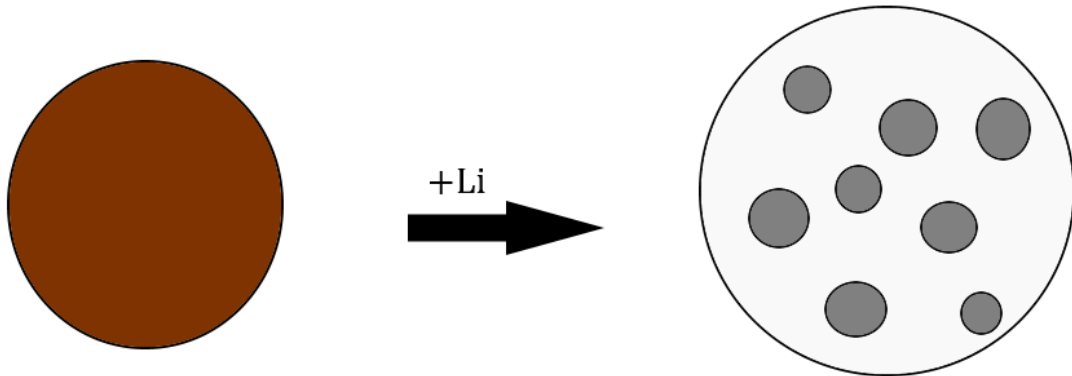


Figure 3.3: A metal oxide conversion active particle is converted into an amorphous Li_2O phase with metal particles embedded into it.

SnO_2 and SiO_2 are materials that undergo conversion followed by alloying. The metal

oxide follows the typical conversion reaction forming LiO_2 . The metal particles that separate during this reaction are now able to alloy with new Li ions that diffuse into the anode. Resulting in the exact alloying reaction 3.2 forming LiM alloys. The initial conversion reaction can be considered irreversible for bulk or large particles, which is why these materials are often classified as alloying rather than conversion. Because of this, these types of metal oxides have high capacities like their pure metal counterparts, however, also experience the same issues as their pure metallic counterparts [40].

The remaining interest in oxides as conversion anodes, despite their issues, is due to their abundance and lower processing cost. They are the end product of the natural oxidation of metals, which simplifies the processing of the raw materials. Even anodes made from Fe_2O_3 and Fe_3O_4 , which are found in regular iron ores, have a good theoretical capacity [41].

3.5 Cobalt Based Anodes

The ZIFs that are investigated contain Cobalt, so understanding the role of Cobalt in anode materials can give some insight in the expected behaviour of the ZIFs during the lithiation process.

The role of Co in anodes is to modify the properties of the anode, rather than directly interacting with the Li ions. Co is inert towards Li ions, meaning that it can only be used in anodes where a different atom or molecule is capable of binding the Li ions. Co is used in intercalation cathodes, where it influences the Fermi level of the cathode, and is not directly of importance to the intercalation process, as it can be replaced by other transition metals such as Nickel and Iron. While Co cannot be directly alloyed to Li, it can be used as a component in alloys that function closer to conversion reactions. An alloy of Co and Sn react with Li ions to form a Li and Sn alloy, while Co metal is separated out in the reaction



where the newly formed alloy can bind additional Li ions alloy until it reaches the earlier mentioned composition $\text{Li}_{4.4}\text{Sn}$.

There are two forms of cobalt oxide that are used as anode material. Cobalt(II) oxide (CoO) and cobalt(II,III) oxide (Co_3O_4). CoO comes in a rocksalt crystal structure, while Co_3O_4 assumes a spinel structure, with Co(III) in the two octahedral positions and Co(II) in the tetrahedral position. Co_3O_4 is the more abundant of the two oxides and is more often used in research. Due to the spinel structure, the conversion reaction undergoes intermediate steps where CoO forms, however, the end result is similar, with a complete separation of the Co and the formation of Li_2O



The cobalt oxide conversion anodes have the same upsides and downsides as any other conversion anode. They exhibit high initial capacity (890 mAh/g for Co_3O_4) and are cheaper and easier to produce than their pure metal counterparts, however, suffer from

volume expansion (approx. 100%), low reversibility of the initial lithiation reaction, low electron conductivity (considered semi-conductors), and poor cycling stability due to active particle aggregation [42]. The average potential is fairly high due to a plateau at 1V, resulting in a lower OCV compared to other anode materials. The most common approach to improving the anodes is related to forming a composite of a good electron conducting material with nano-sized Co_3O_4 particles embedded. The composite acts as a more rigid binder to prevent aggregation of the particles, which is considered a prevalent issue for Co_3O_4 anodes.

3.6 Order-Disorder Materials

The chemical reactions in amorphous materials does not differ from their crystalline counterparts, and the differences arise from structural differences instead. The differences between glassy materials and crystalline materials will be discussed in more detail in section [Properties of Glass]

3.6.1 Summary

The future prospect for anodes seems to be using various additives and modifications to alleviate the issues of volume expansion and SEI stability during the alloying or conversion reactions. The two types have different strength and weaknesses. Alloying materials have worse ionic conductivity, while conversion materials have worse electron conductivity and greater issues with reversibility [43].

A common trend in anode development is creating composite anodes with a nano-sized active material. Carbon based additives have properties that enhance anode properties such as electronic conductivity, flexibility to alleviate stress, as well as acting as a secondary active material, while forming a matrix with the primary active material. Polymer binders can help alleviate the stress further, while reducing aggregation of the active material, creating a more homogeneous anode. The active material on its own cannot act as a stable anode, so the additives are necessary for anodes to maintain a high CE for 1000 or more cycles.

Many of the modifications made to the active materials reflect what we know from section [Theoretical Summary]. Nano-sized structures of the active material are used to improve thermodynamic and kinetic properties, such as the potential profile and reversibility of the lithiation. The surface area of the active material is increased to allow a greater diffusion from the electrolyte to the solid. Additives are used to improve electron conduction and maintain the homogeneity of the anode, to reduce polarization losses.

Recent news related to EVs shows the slow incorporation of Si metal into commercial anodes in the form of using a combination of graphite and silicon active particles in the same anode. Research from 2013 [44] on graphite with added Si at 5 wt% showed that a small amount of amorphous Si powder was enough to improve the practical capacity, even when applying strong currents. Polymer binders are used to maintain structural integrity of the anode, as the Si still undergoes the same volume expansion. Tesla mentioned during a press conference in November 2020 that their new anodes will include 30% Si, not including any specific details, other than using low-quality Si to decrease the cost [45].

It was mentioned that Li plating becomes an issue, especially during fast charging. The addition of the Si particles can quickly react with Li ions to decrease the concentration and reverse plating that has already occurred. A white paper by Sila Nanotechnologies released in October 2020 emphasised a shift towards developing binders, coatings and other additives, rather than looking for alternative active materials [7]. The main focus of both Sila and Tesla was reducing the price to energy density ratio ($\$/kWh$) of anodes, as it is the easiest way to increase the market viability of EVs.

Based on this information, in the short-term, anodes that are used for commercial use will focus on modifying graphite based anodes with the current active materials and additives. Research itself will likely still focus on finding a way to create anodes fully consisting of alloying or conversion materials. New findings can then be used to gradually improve the graphite anodes.

3.7 Zeolitic Imidazolate Frameworks as Anodes

This section will review the properties of ZIFs and in particular the two ZIFs that are investigated (ZIF-62(Co) and ZIF-67). Then how their properties relate to their performance as anode active materials will be discussed.

Zeolitic imidazole framework (ZIF) is a subset of metal-organic frameworks (MOFs) that form crystals with topologies that adhere to corner sharing tetrahedrons. Each tetrahedral unit consist of metal cation in the center. The bridges that connect the tetrahedral units are imidazole and imidazole derivatives. The bonding angle between each tetrahedral unit is 145° , due to the internal angle between of the two lone pairs in the imidazole type molecules. This is similar to bonding angle of zeolites, which is the origin of the name ZIF. Although ZIFs have many of the same topologies as zeolites, ZIFs are not restricted to those topologies.

Just like all MOFs, ZIF crystals are formed from the coordination bonds between metal cations and imidazole anions. One aspect that makes ZIFs interesting is the relative size between the oxygen bridges in conventional zeolites and the imidazole linkers in ZIFs. The cationic node and anionic linker structure results in comparatively larger units. The result is familiar topologies that are enlarged. Since everything is enlarged, so is the volume between the units, resulting in a greater pore volume, greater pore sizes and overall lower density. Both the metal nodes and the imidazole linkers can act as chemically active sites, which are more accessible than in other crystalline materials due to the porosity of the crystal structure. Some of the commonly cited uses for ZIFs are gas absorption (including carbon capture), as sensors for specific metal ions, and as molecular sieves capable of separating CO_2 from other gasses [46, 47].

Most MOFs and ZIFs are unable to melt, as the crystal structure is stronger than the covalent bonds of the organic linker molecules, resulting in thermal decomposition before melting can occur. These aspects will be explained in greater detail in the Chapter 4, however, a short description would be that the amorphous state of ZIFs exhibit an increase in density, rather than the usual decrease in density. While the total pore volume might decrease slightly, the accessible pore volume might be the same if not slightly larger, due to the rearrangement of bonds. This rearrangement also causes the size of the

pores to deviate, creating some pores that are larger in the glass than in the crystalline arrangement.

3.7.1 ZIF-62(Co)

ZIF-62 is similar to ZIF-4, consisting of regular Imidazole linkers, where 1 out of 8 linkers is in the structure is substituted with Benzimidazole. The only difference for ZIF-62(Co) is that the Zinc cations are replaced by Cobalt cations. The ideal chemical formula, based on ZIF-62, is written as $Co(Im_{1.75}bIm_{0.25})$ describing the ratio between Cobalt nodes and the two types of linkers. Based on $^1H - NMR$ results, the actual composition of the Co version is closer to $Co(Im_{1.65}bIm_{0.35})$. Based on DFT simulations for ZIF-62, this slight change in the linker ratio, can lead to differences in the density of the glass made from ZIF-62 after melt-quenching, compared to the regular 1.75:0.25 ratio [48]. ZIF-62 has the same topology as ZIF-4, being the non-zeolitic cag topology. The density of ZIF-62 is $1.49 g/cm^3$. It is difficult to find sources that agree of the window and cavity size for ZIF-62. PALS suggests 2.5 \AA as the largest cavity diameter. Gas adsorption studies show that ZIF-62 has an affinity for adsorbing O_2 , which has a kinetic diameter of 3.4 \AA . Simulations of ZIF-62 predict a cavity size of 4.6 \AA with window diameters of 1.4 \AA . Generally the cag topology is dense, and these pore sizes reflect that [46, 47, 49].

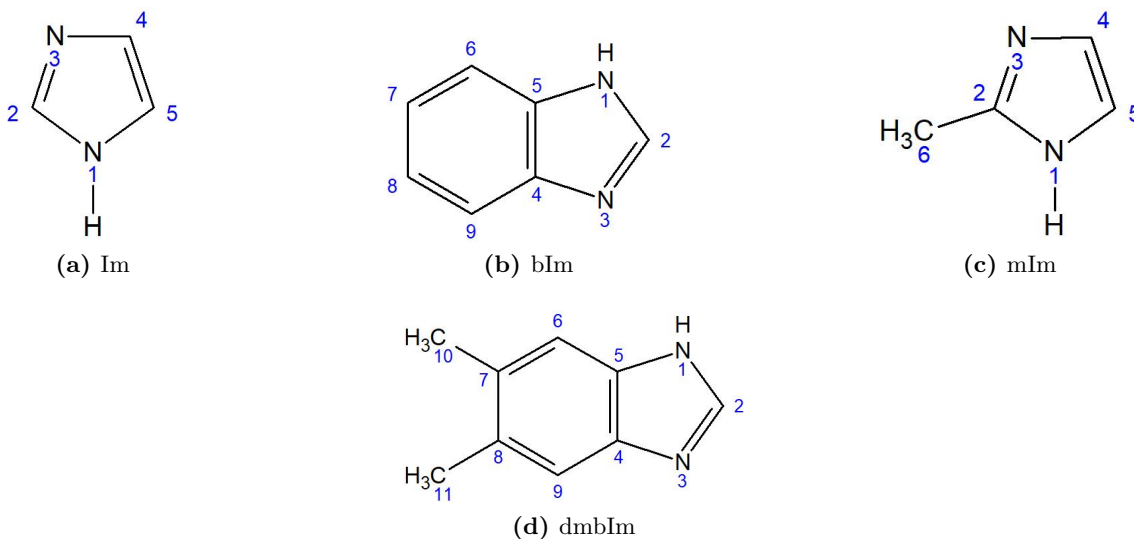


Figure 3.4: The molecular structure of Im, bIm, dmbIm and mIm, respectively.

3.7.2 ZIF-67

ZIF-67 has the same structure as ZIF-8, however, the cationic nodes consist of Co instead of Zn. The anionic linker used is exclusively 2-methyl-imidazole. The crystalline structure of ZIF-8 has the zeolitic SOD topology. The window size of the pores is 3.4 \AA and the largest cavity diameter is 11.6 \AA . The density is lower than other ZIFs with the SOD topology at $0.95 g/cm^3$. This is reflected in the pore volume, which is greater than other ZIFs with the SOD topology. The SOD topology is a very stable topology, having a higher mechanical stability and lower thermal expansion than other zeolite topologies with similar pore volume. These properties are also reflected in the inability of ZIF-8 and ZIF-67 to

melt before decomposing [49–53]. Therefore, instead of melt-quenching, ball-milling has been used to turn ZIF-8 and ZIF-67 amorphous. One article reported that the BET surface area of ZIF-67 is greater than that of ZIF-8 at 749 and 1204 m^2/g respectively [54].

3.7.3 Predicted Anode Behaviour

Research on how ZIFs perform as the main active material in anodes is almost non-existent. ZIF is more often used in a slightly different context. A few examples are as following, the pores of the ZIF are used as nano-sized moulds for a different active material, or as precursors for oxide nanoparticles [55] using the same conversion as reaction 3.5, or protective layers for other anode materials [56]. A single article measured the capacity and cycling stability of an unnamed Zn based ZIF with imidazole and 2-amino-benzimidazole (abIm) as linkers with the composition $Zn_2(Im_{1.5}abIm_{0.5})$. The specific capacity was low at 80 mAh/g at a current of 400 mA/g . It did show a gradual increase in the capacity over the 200 cycles, especially at lower currents of 100 mA/g . XRD measurements after the 200 cycles did not show any clear signs of amorphisation [10].

Cobalt was mentioned in the previous section, and is not going to act as the Li binding agent, which means that the imidazole linkers are going to be the molecules that bind with the Li ions. Modified imidazolates have been experimented with as alternative electrolytes for LIBs, but not as an active material. An article by Yu et al. did note that the ZIF-8 protective layer did also participate in the lithiation process, where NMR signals of the lithiated state indicated that a change in the chemical environment of mIm linkers had occurred [56]. Since the layer consisted of ZIF-8, and not ZIF-67, it is important to note that Zn metal can alloy with Li, whereas Co metal cannot, in case the change in chemical environment is related to the Zn, rather than the imidazole. A different article by Scheers et al. studied various imidazole derivatives as electrolytes for LIBs [57]. The implications of the article would mean that imidazole can bind Li ions, however, in the context of an electrolyte and not as an anode storing Li ions.

The main proposed mechanism for lithiation in all MOFs is intercalation. Most linkers consist of aromatic rings, due to their rigidity, and heteroatoms that can form the coordination bonds with the metal nodes. This allows for π interactions between the Li ions and the aromatic rings, similarly to how the intercalation occurs in graphite. A question that has to be addressed is the charge neutrality of the lithiated state. Graphite stores electrons in the π band of the graphene layers. Si and Sn store electrons in bonds with some covalent character. Conversion and intercalation materials, with transition metals, store electrons in the 3d orbitals of the metal. A single

The partially negative charge at the heteroatoms could also attract Li ions, although it would be a fairly weak interaction without fully breaking the coordination bond first. This is in itself also a problem, as it can destroy the entire structure. , The theoretical capacity of ZIF based active materials can vary based on the

If ZIFs with Cobalt metal nodes are to function in similar ways as other ionic cobalt anodes, there should occur a conversion reaction, where the Li ions can interact with the negative charge of the imidazolate linkers. The conversion will cause an isolation of the

Co, which may result in the same phase separation as for other conversion type cobalt anodes,



where the assumption of a single linker pairing with a single Li ion is based on the proposed interaction between imidazole and Li ions in imidazole based electrolytes [57].

If the assumption of a conversion reaction is correct, then there could be a concern regarding the release of imidazole linkers into the electrolyte. While ZIFs are not very soluble in organic solvents, the linkers are when freed from the crystal structure. Conversion reactions rely on restructuring of the material and could lead to leaking of the active material into the electrolyte after many charge-discharge cycles.

Most ionic Cobalt anodes have low electron conductivity, which can become an issue if higher current densities are applied to the battery, resulting in greater Joule heating and drop in OCV. With regards to ZIF based materials specifically, the cobalt based ZIFs have superior electron conductivity when compared to their zinc counterparts [58]. The proposed reason for the difference in electron conductivity is related to the $3d^7$ orbital of cobalt. Zinc has a filled $3d^{10}$ orbital, making ionisation beyond the $4s^2$ orbital unfavourable. This limits zinc to a oxidation state of II, while cobalt is able to assume III, IV and V as well. In this case only the III state is of importance for the electron conduction, as it allows charge to hop more easily with an easily available oxidised state.

The purpose of the glassy nature of the anode can be considered as an attempt to figure out how amorphous materials change the properties of the active material. While electron conductivity and capacity should not be significantly changed, there might be changes to ion conductivity and conversion process during lithium ions intercalation. The aspects of glass, and what it might change will be explained in the following section.

3.7.3.1 Summary and Perspective

Currently there is almost no concrete information on ZIFs as standalone anodes. From the basic principles of the various Li storing principles. ZIFs would fall into the category of conversion anodes. It does not have the strong bonding that graphene has, so the Li ions would likely interact strongly with the negative electron density of the imidazole, while the cobalt would be reduced by the electrons supplied by the circuit. Alloying can be ruled out, since cobalt does not bond like Si and Sn do.

The low electron conductivity in ZIFs is can become a limiting factor, if the other processes are faster. Something that should not be ruled out is that Li plating can occur, if it is more favourable.

The goal of the project is to look into the performance of glassy materials with different structural properties, and therefore this section will explore the properties of glass in comparison to crystalline materials, and how these properties are further influenced by the conditions of glass formation.

4.1 Thermodynamics of Solids and the Amorphisation Process

For crystalline materials the Gibbs free energy is a description of whether the material is in an equilibrium state, or in a non-equilibrium state. The absolute value of the entropy (S) is related to the number of available energy states of the material. It can be called an intrinsic value that only changes when the structure itself changes. The connection between the structure and entropy can be seen through various relations, such as with the heat capacity $\Delta S = \int (C_p/T)dT$, and first order transitions $\Delta S = \Delta H/T$. ΔS is the change in entropy, C_p is the isobaric heat capacity, T is the absolute temperature, and ΔH is the change in enthalpy.

The equation for Gibbs free energy

$$\Delta G = \Delta H - T\Delta S, \tag{4.1}$$

gives a relation of how equilibrium is maintained as the temperature of a material increases. The change in entropy (ΔS) in a material will always be positive with increasing temperature (since $S(T_2) > S(T_1)$ for $T_2 > T_1$), which means that the ΔH also has to be positive to maintain the equilibrium.

ΔH can be considered the change in energy during a bond breaking and subsequent migration process in the material. The perfect crystal has a lower enthalpy relative to a crystal with defects, and since $\Delta H > 0$ to maintain equilibrium, the process of breaking bonds and creating defects increases as the temperature increases. The formation of defects is akin to the mixing entropy in section 2.2.1, where defects are considered dissolved in the solid material. This is often considered as the configurational entropy of a material. The decrease in bonding and increase in defects leads to instability and finally the destruction of the crystal lattice when reaching a critical temperature, which results in a first order phase transition also known as the melting process. Cooling the material back below the critical temperature results in the reformation of the bonds resulting in the crystallisation process. The number of bonds for crystalline materials can more accurately be described as the average coordination of the atoms that make

up the crystal. Where the theoretical coordination number is for the perfect crystal without any intrinsic defects. This remains consistent with the Lindemann criterion, where melting is proposed to be caused by an increase in the average distance between atoms. Less bonds and lower coordination are caused by vacancies and defects, which also would increase the average distance between atoms. It should be noted that liquids still have average coordination close to that of a solid, and only enough bonds are broken to cause the collapse of the crystalline structure. For a material consisting of tetrahedral units the average coordination would remain close but slightly below 4 [59]. The structural definitions of short range and long range order are often useful to describe the differences between crystals and liquids. Short range order is maintained, meaning that coordination to nearest neighbour atoms, bond lengths and bond angles remains intact, although often with greater deviation from the equilibrium values in all three. The increase in the deviations cause a break down of the long range order, as the structure no longer resembles an infinitely repeating structure.

Applying the same bonding description of thermodynamics to amorphous materials, glass can be considered a solid in a thermodynamic meta-stable state, where the number of bonds does not correspond to the equilibrium state of the crystalline phase. The two methods that will be considered to create amorphous materials are melt-quenching and ball-milling. Ball-milling applies varying shear and tensile stress against the crystal that crush and deform the crystal particles. The type of defects that result from milling are line and surface defects. Decreased particle size and formation of cracks increases the surface area, which are considered as defects. Many of the crystal planes are likely dislocated in the form of line defects. Ball-milling does not turn the material into glass as it typically is known, it instead reduces the signals that characterise crystals to the point that it can no longer be identified. Examples would be the to loss of constructive interference when measuring Bragg diffraction with X-ray scattering, meaning that the presence of detectable crystals has disappeared and the material can be considered amorphous.

Melt-quenching forms amorphous structures, as the name suggests, by first disrupting the crystalline structure by melting, followed by cooling. The cooling process brings the temperature of the melt below the melting point turning the melt into a super-cooled liquid. The cooling rate has to increase the dynamic viscosity (η) of the melt to a point where self-diffusion processes occur far slower than the kinetics of crystal growth (which is inversely proportional to η through the Stokes-Einstein relation) to maintain the super-cooled liquid. Crystal nucleation is allowed to occur, so long as the growth of the crystals is slow and does not reach the critical size where growth becomes thermodynamically favourable. The energy of nucleation and growth of the crystals initially decrease when cooled below the melting point, due to the increasing difference in Gibbs energy between the liquid and crystal states. However, the energy required for self-diffusion increases faster the further the temperature drops below the melting point. The result is that the nucleation and growth rate drop and the melt is vitrified into the glass state. The difference between melt-quenching and ball-milling are very noteworthy, as the approach results in very different types of structures and defects. Melt-quenching does not increase surface defects, it instead freezes the intrinsic defects of the liquid state into a thermodynamically meta-stable solid. The intrinsic defects being points defects and the loss of long range order. The differences in the structure can be summed up as finely crushed crystalline

powder and frozen liquid.

4.2 Annealing and the Structure of Glass

4.2.1 Entropy and Glass Structure

The glass transition is a second order transition where the heat-capacity of the material changes in a continuous manner over a short temperature range. Since glass in many regards can be considered liquid structure, where the crystalline order already is broken, there is no longer a typical first order melting process. Instead of melting, the glass undergoes a continuous change in physical properties during the glass transition. Below the glass transition temperature (T_g) glass behaves more as a solid, while above T_g it behaves as a super-cooled liquid. When using the energy dispersion description of entropy, the glass transition can be considered as a point where additional modes for energy dispersal become available. This increased dispersion is often called an increase in configurational entropy. The glass transition for polymers gives an easier to grasp picture of this, where going above T_g allows for increased mobility of pendant groups. The increased mobility unlocks additional modes for kinetic motion and energy dispersal, thereby increasing the entropy. The increased movement can also be classified as an increase in the degrees of freedom. Since the polymer glass transition is slightly different from the glass-liquid transition, it would be more accurate to ascribe the change in configurational entropy to an increase in vibrational modes of the structure, or an increase in the freedom of atoms to move within the structure. Both can be linked to the observed increase in heat capacity during the glass to liquid transition, through either the Debye model for solids or the equipartition theorem applied to liquids. Either approach indicates an increase of motion within the material at the glass transition.

The potential energy landscape describes the entropy of glass and super cooled liquids in two separate components related to the basins that make up the PEL. It consists of basins with multiple microstates in each basin. Inter-basin relaxation refers to a material being able to explore multiple basins and is the relaxation that becomes frozen when cooling a super-cooled liquid into the glassy state. Intra-basin relaxation refers to the exploration of the various states that make up a single basin. Glass still experiences the intra-basin relaxation even if inter-basin relaxation is frozen. The two relaxations are related to the configurational and vibrational entropy respectively. Where the configurational entropy vanishes as the inter-basin relaxation is frozen. The vibrational entropy remains but vanishes as the temperature decreases towards 0 Kelvin.

4.2.2 Annealing

The purpose of annealing is to heat a material to a temperature where thermally activated processes occur more often, and to maintain that temperature to allow the processes to occur for longer[cite book]. Increasing self-diffusion is the main purpose of most annealing procedures, as it allows atoms to migrate and rearrange into the equilibrium structure of the material. The rearrangement decreases the structural defects of the material, which is why it often is used relieve stress in glass or improve the ductility of metals and alloys. The remaining intrinsic defects should decrease when the material is cooled back to room-

temperature. The self-diffusion depends on the viscosity of the material, so the success of annealing similarly depends on heating to the right temperature for a long enough period of time. Understanding the glass transition is important in the case of annealing glass, as it is the point where a glass-liquid transition changes the physical properties and also allows viscosity models to describe the viscosity of the material [cite viscosity models].

From a PEL description, the increase in the temperature during annealing decreases the relaxation time of inter-basin transitions (secondary relaxation), described by the KohlrauschWilliamsWatts (KWW) equation. The glass is allowed to explore the various configurations that make up the PEL, resulting in the glass assuming a lower energy configuration. This is why annealing and aging are both used as terms for the process. The heating allows the glass to relax (age) faster than it at lower temperatures. Whether the aging process actually occurs still depends on the diffusion processes. If the activation energy of the diffusion process is too high, even above T_g , the relaxation time will be long, and the increased temperature is not enough to activate the relaxation process. Whether the structural change has occurred during annealing can be determined when performing a DSC upscan. Any pre- T_g exothermic events that would happen in the non-annealed glass should already have occurred during annealing, and the magnitude of the glass transition itself should be sharper with a greater enthalpy, as the relaxed glass structure is returned to the super-cooled liquid state. Annealing can be said to lower the fictive temperature of the glass retroactively by releasing some of the excess enthalpy [34, 60, 61].

A common representation of the melt-quenching process describes glass as having a higher enthalpy and volume, when compared to the theoretical super-cooled liquid at the same temperature. Faster quenching rates leads to a greater difference in volume between the two, while aging of the glass reduces the volume [62]. The expected outcome of an annealing process is that the volume decreases, and therefore the density of the glass increases during annealing. While density is not always directly related to the self-diffusion of species within dense glassy materials, there is a relation between the free-volume and the diffusion within metals, liquids and polymers based on the work of Cohen and Turnbull [63]. A key distinction is that these materials do not consist of a continuous network of covalent bonds. However, the energy of self-diffusion is the combined desorption and migration, regardless whether it is within the crystal lattice or on a surface. The energy of migration is greater for materials where the diffusing species experiences greater steric hindrance [64]. Material that are less dense should have more open structures allowing for greater self-diffusion, unless the denser material has channels that allow for faster diffusion. The importance of self-diffusion goes back to the Nernst-Einstein relation (eq. 2.24), where the ionic conductivity of a species is related to the self-diffusion of the material.

4.3 Annealing of ZIF-62

The issue with ZIF-62 is that the density of the glassy state is lower than the crystalline state. This is related to the earlier mentioned porosity as a result of the metal node and linker structure. The distance between the nodes of the crystal structure are greater than that of regular crystals. Compared to the usual melting process, where the average distance between atoms increases in the liquid state, ZIF-62 experiences an increased distance between the metal nodes and the linkers causing a structural collapse. It is

therefore not defying the principle of increasing average distance between bonds, however, the pore volume of the crystal state has been lost. ZIF-62 has a high viscosity [65] and low thermodynamic driving force for crystallisation [34], preventing the solidification of ZIF-62 into the original crystal structure. The low thermodynamic driving force of crystal nucleation is likely related to the same reason why ZIF-62 is able to melt before reaching the decomposition temperature. The reason being the stressed nature of the crystal structure and the more relaxed nature of the glassy state [66].

These aspects of ZIF-62, that also apply to ZIF-62(Co), likely mean that annealing does not significantly change the structure, nor will it be able to regain some of the porosity. Annealing ZIF-62 for 24 hours has shown that the structure does relax, measured as an increase in the enthalpy of the glass transition after annealing. Atomic pair distribution function analysis of the annealed ZIF-62 confirmed no difference in short range order (nearest neighbour metal node), and only a very slightly change in the intermediate range order (next-nearest metal node) as a result of densification [34]. Instead of the glassy ZIF-62 relaxing into a structure that closer resembles the crystal state, it instead relaxes into a even more dense state. This still follows the general idea that annealing decreases the volume of the glass and tries to reach the state of the equilibrium super-cooled liquid.

4.4 Expected Changes in Electrochemical Performance

The densification of the glassy state and the further densification of the annealed glass have an increased specific capacity, as the pore volume has decreased. The decrease in pore volume is not necessarily bad either, since the micro-pores might not be easily accessible to the electrolyte in the crystalline state. Ball-milling will increase the surface area, which will likely improve the performance due to lower charge-transfer resistance. The electron conductivity of ZIFs is already low [58], so melt-quenching and ball-milling might actually have positive effect on the conductivity. Pores cannot conduct electrons, so a denser material could increase the overall ability for electrons to move, without increasing the absolute conductivity of the material. Ball-milling can increase the contact area with additives that improve the conductivity, again not directly related to the material itself.

Electrochemical Characterisation Methods **5**

5.1 Galvanostatic Charge-Discharge Cycling

The capacity of a battery is measured in total electric charge with the unit [Ah]. The measurement is performed by connecting the battery to a power supply that can both discharge and charge the battery. As the unit for the capacity indicates, the measurement is performed by drawing a constant current until the battery is discharged. The current in ampere multiplied by the time of the experiment in hours, will result in the capacity. The voltage will drop during discharge. The measurement is usually performed until the cutoff voltage of the specific cell configuration is reached, to prevent permanent damage.

The measurement will result in a discharge curve, which shows the changes in the cell potential as the SOC changes. The shape of the curve can tell us about the lithiation process at different points during charging and discharging as mentioned in section 2.2.1. Usually the capacity axis is the same during charging and discharging experiments. This means that during charging it is the measurement of current supplied to the battery, and during discharging it measures the current drained from the battery. Whether it is a charging or discharging plot can be seen from the slope of the potential. For anodes the potential increases (vs. Li/Li^+) during discharge, and increases during charging. If the total cell potential is shown, it will decrease during discharge, and increase during charging.

5.1.0.1 Cycling

Performing many discharging and charging experiments continuously will give a picture of long-term performance of the cell. The experiment should preferably continue for 1000 cycles while applying increasingly stronger currents. While graphite anodes degrade slowly and consistently with each cycle, this is not a guaranteed behaviour for all anodes. Certain cells show a loss of capacity at seemingly random cycle numbers. Varying the current is also important due to phenomena mentioned in section 2.3, the cycling stability might be good at low currents, whereas it could degrade even within a few cycles at stronger currents. For all anodes it is expected that the capacity will decrease with increased current, while the cycling stability remains unknown until measured. Instability at higher currents can be caused by additional side reactions, which might be specific to that anode material. If these side reactions repeat often enough, it can lead to formation of defects in the anode, causing a rapid permanent decline of the capacity.

5.1.0.2 Coulombic Efficiency

The coulombic efficiency describes the ratio between the current that is supplied to the battery, and the current is released by the battery. It describes the loss of charge during a cycle. Any current lost to processes that are not intercalation will be considered in the CE. Often the first cycle will have a low CE, as charge is lost during the formation of the initial SEI. The CE will also depend on Ohmic losses, meaning that temperature and the strength of the current will influence the value.

5.2 Electrochemical Impedance Spectroscopy

Batteries do not generate alternating current, however, by inducing alternating current within the battery, it becomes possible to observe and quantify the electrochemical properties of the battery. While it is not possible to decouple the contribution from the different components of the battery, Electrochemical Impedance Spectroscopy (EIS) still remains a very useful analysis method.

EIS measures the current response of the cell when applying an alternating current. With Ohms law the inputs can be converted into a complex resistance, which is called the impedance. Impedance is a catch all term for all electric effects that interfere with the flow of charges within a circuit. LIBs experience resistance caused by the material specific mobility of electrons and ions within the various parts of the battery, as well as impedance caused by a build-up of charges at grain boundaries and interfaces where double layers form [67].

Ohms law for impedance is,

$$Z(\omega) = \frac{V(\omega)}{I(\omega)}, \quad (5.1)$$

where the angular frequency ω describes the phase of the applied voltage V and the resulting alternating current I . The main difference is that the impedance Z is a complex number,

$$Z(\omega) = Z'(\omega) + iZ''(\omega), \quad (5.2)$$

where the single mark indicates the real part, and the double mark indicates the imaginary part. During the experiment only the frequency of the potential is changed, while the current is measured as a response to the changing phase and frequency of the potential.

To calculate the impedance of a battery an equivalent circuit has to be setup. The equivalent circuit is supposed to describe the various components and the electrical effects that occur in each of them. It is difficult to predict which circuit will accurately describe the cell, but a common, and the simplest circuit used to describe LIBs is the Randles circuit (depicted in fig. 5.1).

Randles Circuit

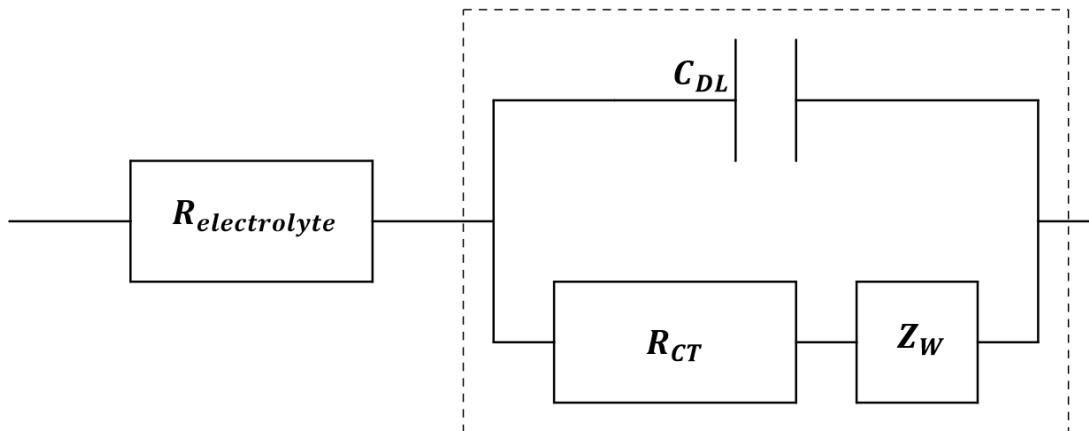


Figure 5.1: Depiction of a standard Randles circuit. The various elements can be switched out in the case where this circuit does not properly fit onto the EIS data.

It describes the primary processes that occur in any LIB. Whether the component contributes to the real or imaginary part of the impedance, depend on how they influence the current. Since the current will have a phase, due to the changing polarity of the potential. The resistance will influence the current at different points during the phase. Real impedance means an immediate response (in phase), while imaginary impedance means a delayed response (out of phase).

The ionic resistance of the electrolyte is described as a single resistor, resulting only in a real impedance. It is in series with the other component, similarly how the electrolyte is in a layered structure between the electrodes. The electrodes with the active material are described by the rest of the components. The capacitor describes the build-up of charges at the double layer where the electrode and the electrolyte meet. Capacitors only contribute to the imaginary part of the impedance, due to how the accumulation and depletion of surface charges (capacitive current) is out of phase with the applied potential. In many cases the capacitor behaviour is not congruent with the behaviour of the cell, and a constant phase element is used instead. The resistor describes the charge transfer resistance, which is related to the kinetics of the lithiation and delithiation reaction. The lithiation reactions require or release electrons, and so will act in phase with the current. The Warburg element contributes equally to the real and imaginary impedance. It is generally attributed to the diffusion process within the electrodes, which is why it is in series with the charge transfer resistance. In cases where the electrode is thin and the current is blocked by a surface, the open Warburg impedance is used. It describes a point where the real impedance does not increase any further, and a build-up of charges causes

an increase in imaginary impedance that goes to infinity.

$$\begin{aligned}
 Z_R &= R & (a) \\
 Z_C &= \frac{1}{i\omega C} & (b) \\
 Z_Q &= \frac{1}{Q(i\omega)^n} & (c) \\
 Z_W &= \frac{1}{Y\sqrt{i\omega}} & (d) \\
 Z_O &= \frac{1}{Y\sqrt{i\omega}} \coth(B\sqrt{i\omega}) & (e)
 \end{aligned} \tag{5.3}$$

The most common graphical representation of EIS data is in the form of the Nyquist plot. It has a distinct shape that ideally resembles the sketch in fig. 5.2.

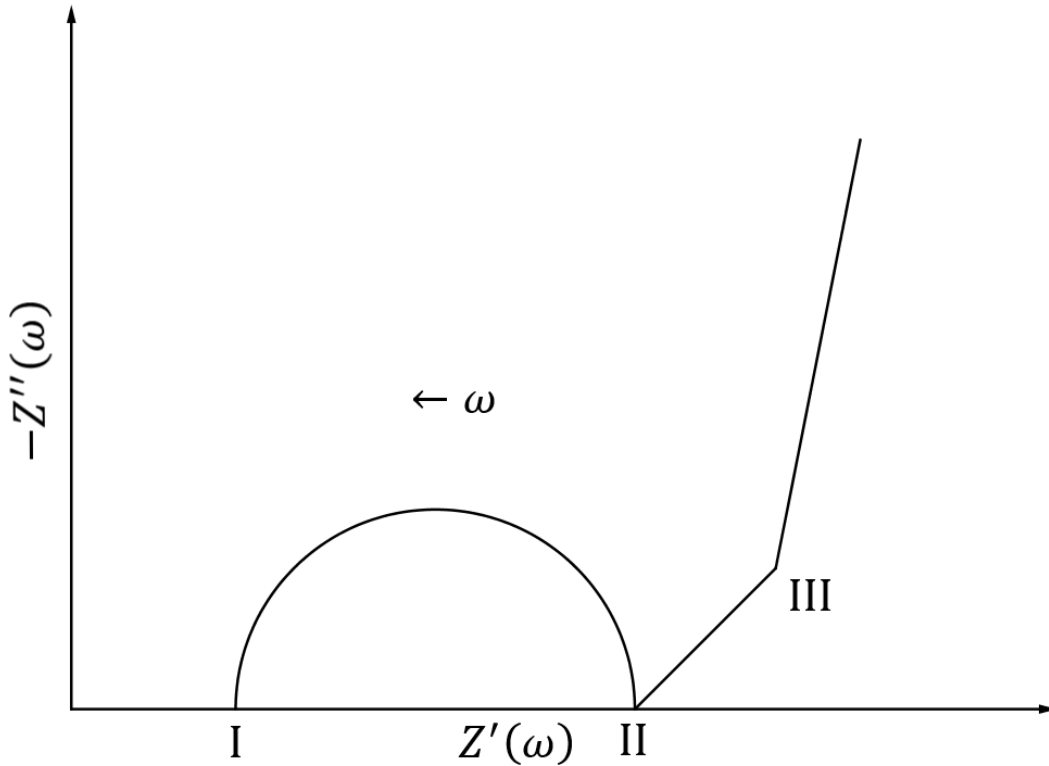


Figure 5.2: Different contributions to the polarization, causing a drop in the working voltage as the current is increased.

The angular frequency of the alternating current is the highest for small values of Z' and decreases when moving along the Z' -axis. A high frequency means that the polarity of the applied electric field switches frequently. This results in short time intervals that are too short for the charge carriers to overcome the over-potential. The beginning of the semi-circle (I) indicates when charges start to move. The real impedance Z' at this point can be considered the Ohmic resistance of the electrolyte that causes the over-potential. The semi circle is a result from the parallel setup of a capacitor and a resistor element.

The radius of the semi-circle is related to the frequency dependent imaginary impedance of the capacitor element. The curvature depends on how much the real impedance increases as the capacitor element. The end of the semi-circle (II) is the combined Ohmic and charge transfer resistance and is related to the resistance experienced when all stored charges on the double layer are removed and the faradaic current takes over from the capacitive current. The first section of the slope at a 45° angle (III) is the Warburg impedance and can be used to roughly determine the mobility of the Li ions in the cell. The final part of the slope has a strongly increased imaginary impedance Z'' related to the thickness of the electrode. Thin electrodes have a finite length for diffusion and do not have the length to increase the real impedance any further at low frequencies.

The Warburg element eq. 5.3(d) is often written as $Z_W = \sigma\omega^{-1/2} + i\sigma\omega^{-1/2}$, where real and imaginary impedance increase at an equal rate, resulting in the 45° angled slope in a Nyquist plot. σ is a constant that can be determined by plotting $\omega^{-1/2}$ vs. $Z'(\omega)$ or $Z''(\omega)$ and finding the linear relation for the values of ω and $Z'(\omega)$ that corresponds to area between II and III in fig. 5.2. The relation between σ and the physical properties is given as

$$\sigma = \frac{RT}{F^2 A \sqrt{2} c_{Li^+} D_{Li^+}}, \quad (5.4)$$

where A is the surface area of the electrode, F is Faraday's constant, c_{Li^+} is the concentration of Li ions in the electrode, and D_{Li^+} would be the EIS determined diffusion of Li ions in the electrode [67]. Higher values of σ increase the impedance of the cell, so it is not surprising that the diffusion of Li ions is inversely proportional with σ .

5.3 Cyclic Voltammetry

Voltammetry is the study of current flow caused by an applied potential. It will measure any type of current that is caused by a change in potential. When using it to study LIBs it can determine at which voltages the Li ion lithiation and delithiation, the SEI formation, and other side reactions occur. It is a useful tool to understand how many electrochemical processes occur and at what voltages these processes happen. Together with the capacity curves it can help the understanding of what happens in the fully assembled cell.

The usual concepts such as the extent of a reaction and the activation energy are directly related to the measured current and the applied voltage. The current corresponds to the number of electrons transferred in the various reduction or oxidation reactions, while changes in the current indicate at which voltage the electrons have enough energy to reduce, or when the electrostatic pull on the electrons is strong enough to oxidise. The positive current is also called the cathodic current, while the negative current is called the anodic current. The cathodic current coincides with reduction reactions (electrons are stored due to the applied potential) while the anodic current coincides with oxidation reactions (electrons are released due to applied potential).

Since voltammetry only applies a voltage, it is able to determine the stability of an anode, when it is exposed to the working potential of the battery. This is especially useful to determine the limits of the active material, and if structural changes occur at certain potentials. Electrochemical reactions often experience a hysteresis in relation to the

applied potential. Cyclic voltammetry can determine at what voltages and the differences when the polarity of the applied potential changes.

Cyclic voltammetry refers to performing a voltammetry scan and performing a second scan with reversed polarity, where the applied potential is decreased back to the initial value of the first scan. How these scans are configured varies, however, for LIB tests the starting potential is just above the Li/Li⁺ electrode potential (-3.04 vs. SHE). The applied voltage is increased until it reaches 3V above the standard Li electrode potential.

Performing multiple cycles gives insight into which peaks were formed due to single time events. These can be caused by irreversible removal of impurities, irreversible reactions of the material, or permanent structural change. The SEI formation is one of these events, if it remains stable upon formation.

Experimental Section 6

6.1 List of Instruments and Materials

Table 6.1: An overview of the used apparatus and their manufacturer.

Apparatus	Manufacturer	Headquarter
Analytic balance (BP 2215)	Sartorius	Gottlingen, Germany
Finn pipettes	Thermo Scientific	Waltham, MA, USA
NMR DRX600 600MHz	Bruker	Billerica Massachusetts, USA
Differential scanning calorimeter (STA448 F3 Jupiter)	Netsch Group	Selb, Germany
Dry Oven (T 5042 EK)	Heraeus	Hanau, Germany
Planetary Ball-mill PM 200	Retsch	Haan, Germany
X-ray diffractometer (Empyrean)	Malvern PANalytical	Malvern, UK
Microscope (Stemi 305)	Zeiss	Jena, Germany
FTIR Spectrometer (Tensor II) USA	Bruker	Billerica

Table 6.2: An overview of the used chemicals and their manufacturer.

Chemicals	Manufacturer	Headquarter
Benzimidazole (98%)	Sigma Aldrich	Steinheim, Germany
Cobalt nitrate hexahydrate ($\leq 95.0\%$)	Sigma Aldrich	Steinheim, Germany
35% Deuterium chloride in deuterated water	Sigma Aldrich	Steinheim, Germany
Dichloromethane	VWR International	Briare, France
2-methylimidazole ($\leq 99\%$)	Sigma Aldrich	Steinheim, Germany
Deuterated dimethyl sulfoxide (99.8%)	VWR International	Leuven, Belgium
Imidazole (99%)	Sigma Aldrich	Steinheim, Germany
N,N-dimethylformamide	VWR International	Briare, France
Methanol	VWR International	Briare, France

6.2 ZIF-62(Co) Synthesis

ZIF-62 (Co) was synthesised using a solvothermal method. 1.2 g (4.1 mmol) cobalt nitrate hexahydrate ($\text{Co}(\text{NO}_3)_2 \cdot 6\text{H}_2\text{O}$) was added to a 200 mL beaker containing 100 mL N,N-

dimethylformamide (DMF). The content was stirred until all the crystals were dissolved, resulting in a purplish-red solution. 0.81 g (11.7 mmol) imidazole, and 0.21 g (1.7 mmol) benzimidazole were added afterwards while maintaining the stirring. Stirring continued until all solids were dissolved. 40 mL of the solution was transferred to a 50 mL autoclave, which was repeated for a total of two autoclaves. An electric oven was preheated to 140 Celsius. Both autoclaves were placed in the oven and heated for 7 days. The autoclaves remained in the oven during the subsequent passive cooling to ambient temperature. The content of the autoclaves consisted of precipitated crystals and the mother solution. The mother solution was carefully removed using a pipette, and the remaining crystals were collected and transferred to a centrifuge tube using DMF. The crystals were washed by adding 20 mL DMF total and vigorously shaking the tube. The tubes were centrifuged at 4500 RPM and the supernatant was removed. This was repeated another time, for a total of two DMF washes. Another wash was performed with dichloromethane (DCM), in the same way, to remove as much of the DMF as possible. After the centrifuge, the DCM was removed, and the content was transferred into a 50 mL glass beaker. The top of the beaker was covered with aluminium foil, with small holes poked into the foil, to allow the DCM to evaporate. The beaker was placed in an oven at 110 Celsius overnight. The resulting crystals were collected and characterised using proton-NMR.

6.3 ZIF-67 Synthesis

ZIF-67 was synthesised using a solvothermal method, based on the synthesis method of ZIF-8. 0.9 g (3.1 mmol) cobalt nitrate hexahydrate ($\text{Co}(\text{NO}_3)_2 \cdot 6\text{H}_2\text{O}$) was added to a 200 mL beaker containing 100 mL DMF. The crystals were stirred until it was fully dissolved. 0.2522 g (3.1 mmol) 2-methylimidazole was added to the solution and stirred until all was dissolved. 40 mL of the solution was transferred to a 50 mL autoclave, which was repeated for a total of two autoclaves. An electric oven was preheated to 140 Celsius. Both autoclaves were placed in the oven and heated for 24 hours.

The content of the autoclaves consisted of mostly mother liquid, with a small amount of crystals. The liquid was carefully removed using a pipette, and the remaining crystals were placed transferred to a beaker using DMF. The

A synthesis using methanol as a solvent was attempted, and while the resulting material was confirmed to be ZIF67 using XRD, the material is not suitable for ball milling.

6.4 ZIF-62(Co) melt-quenching

The ZIF62 crystals were divided into two portions, each containing 300 mg. The crystals were contained in a small glass jar without a lid. The jar was placed in the tube furnace, and the furnace was closed off with an airtight seal. The air atmosphere inside the tube was flushed for 30 minutes using Argon gas. When the flushing was complete, the oven was turned on, the water flow was enabled, and the heating was initiated. The oven heated to just above the melting point of ZIF62 at 700 Kelvin. The temperature was maintained for 1 minute, before cooling began. The cooling was set to 10 Kelvin per minute. The jar was kept in the furnace for an hour after the heating element reached 0 Celsius, to ensure that the jar had cooled down. The second sample had an additional annealing

stage, where after the first cooling, a temperature close to the glass temperature of ZIF62 was maintained for two hours, before regular cooling was continued. XRD confirmed the amorphous state of both samples.

6.5 ZIF-67 ball-milling

400 mg of ZIF67 crystals were added to a crucible together with the marbles used for ball milling. An initial run at 250 RPM for 40 minutes resulted in a fine powder. An XRD of the powder showed a mixed crystalline and glassy signature. The second run was performed on the already milled powder at 270 RPM for 60 minutes. The resulting powder was even finer and XRD showed no clear crystalline signature, indicating that the powder consists of amorphous ZIF67.

6.6 Powder X-ray Diffraction

PXRD was performed at room temperature using PANalytical diffractometer with a Cu K_{α_1} ($\lambda = 1.5406 \text{ \AA}$) X-ray source. Collection conditions were: $2\theta=3-40^\circ$, step size was 0.013° and the time per step was 29.07 s. The slits used for the incident beam path was as follows: 0.04 rad soller slit, 15 mm fixed incident beam mask, 1/8 divergence slit and 1/4 antiscatter slit. The slits used for the diffracted beam path were as follows: 0.04 rad soller slit and 8.0 mm antiscatter slit.

6.7 Liquid Nuclear Magnetic Resonance Spectroscopy

All liquid NMR experiments were carried out on a Bruker DRX600 spectrometer. The ^1H spectra were calibrated using the residual solvent peak, in accordance with the literature [68]. The samples were prepared by dissolving 10-15 mg of the sample in a solvent mixture of 150 μL 35% DCl in D₂O and 750 μL of DMSO (1:5) and $\sim 550 \mu\text{L}$ was transferred to an NMR tube.

6.8 Differential Scanning Calorimetry

DSC is carried out on a Netzsch STA449 F3 Jupiter using Ar as the atmosphere. Sample masses between 10 and 20 mg of the products were measured and recorded for every analysis. Two different DSC analyses were performed on ZIF-62(Co). The first analysis was to investigate a potential melting point of the products. The second analysis was to investigate the T_g the sample. The T_g analysis used a blank baseline and sapphire as reference for the scans to determine C_p . Cooling and heating rates were 10 K/min.

6.9 Other

The samples were sent to Wuhan University for electrochemical testing. I do currently not have any information of the procedure of the testing or exact assembly of the coin cells. Although assembly likely follows the standard procedure of mixing the active material with carbon black and PVDF binder to form a slurry. The slurry is spread on copper foil

and dried. The coins consist of the electrode made from the active material, an insulating polymer separator and a Li chip as the counter electrode.

A lot of the tests did not manage to finish before the hand-in date of the report. The five samples are crystalline ZIF-62(Co), melt-quenched glassy ZIF-62(Co), melt-quenched glassy ZIF-62(Co) annealed for 2 hours, crystalline ZIF-67 and ZIF-67 ball-milled. When referring to the cell, it means a coin cell made with the active material as one electrode and a Li metal chip as the other electrode. Therefore, the active material will behave as a cathode rather than an anode. This also applies to charging and discharging, where discharging is the lithiation of the active material, and charging is the delithiation of the active material.

7.1 Powder X-ray Diffraction

PXRD was used to confirm the expected crystalline structure of ZIF-62(Co) and ZIF-67. The signature weak peaks of ZIF-62(Co) can be seen in fig. 7.1 as well as the disappearance of the peaks after the melt-quenching process, confirming a loss of crystallinity. The 2 hour sub- T_g annealing process did not cause any change. The spectra are for the active materials before cell assembly and the cycling process.

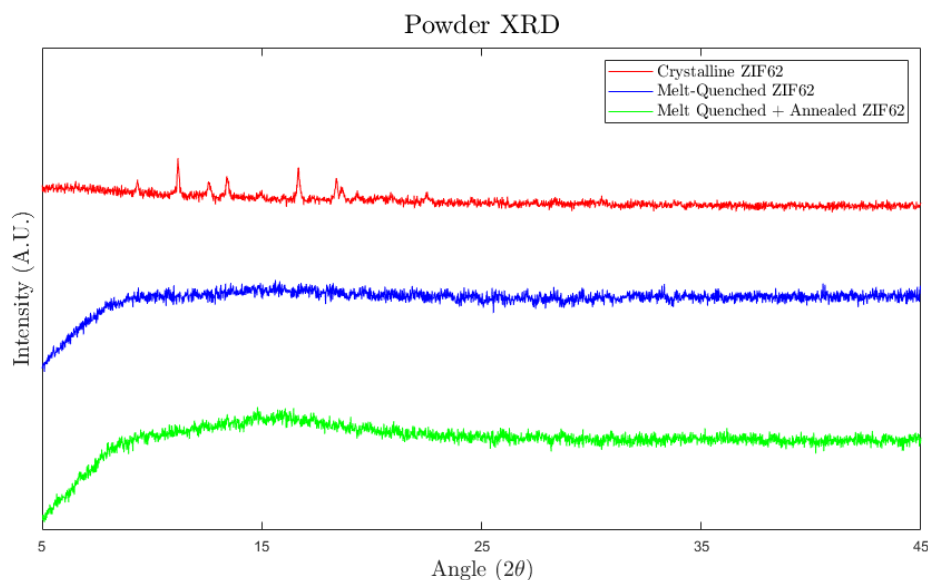


Figure 7.1: PXRD spectra of crystalline (red) and melt-quenched ZIF-62(Co) samples (blue for regular and green for annealed)

The spectrum for crystalline ZIF-67 in fig. (7.2) is far sharper than that of ZIF-62(Co), and the spectrum for the ball-milled ZIF-67 shows no clear sign of Bragg peaks that

correspond with the crystalline ZIF-67.

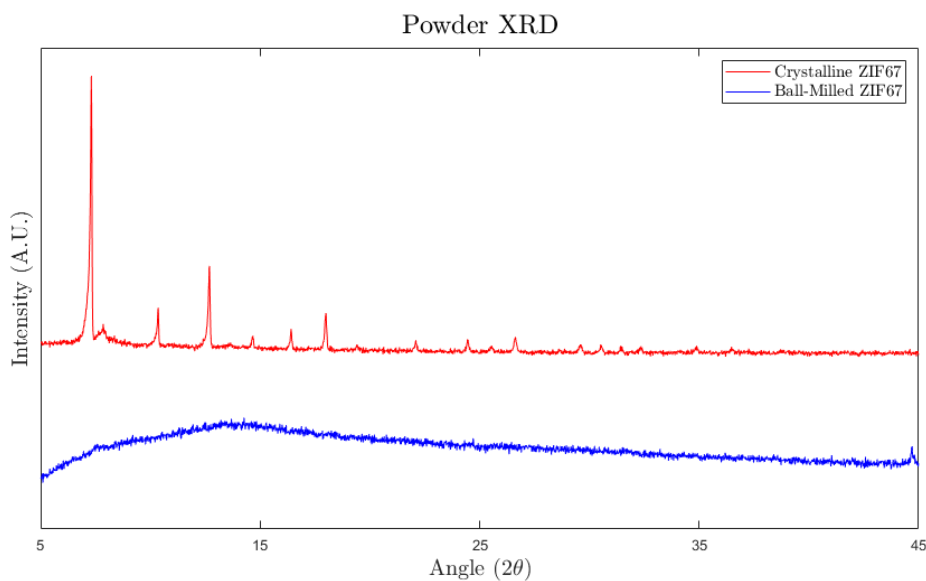


Figure 7.2: PXRD spectra for crystalline (red) and ball-milled (blue) ZIF-67

7.2 Scanning Electron Microscope

SEM was used to confirm the particle shape of the active material before cell assembly. Images for ZIF-62(Co) and melt-quenched ZIF-62(Co) were received. A fully-developed ZIF-62 crystal is shaped like an octahedron. The observed particles are likely to have additional sides due to unfinished development. The images made of the crystalline sample showed no undamaged particles, the best candidate being shown in fig. 7.3, where the octahedral shape is recognisable regardless of damage.

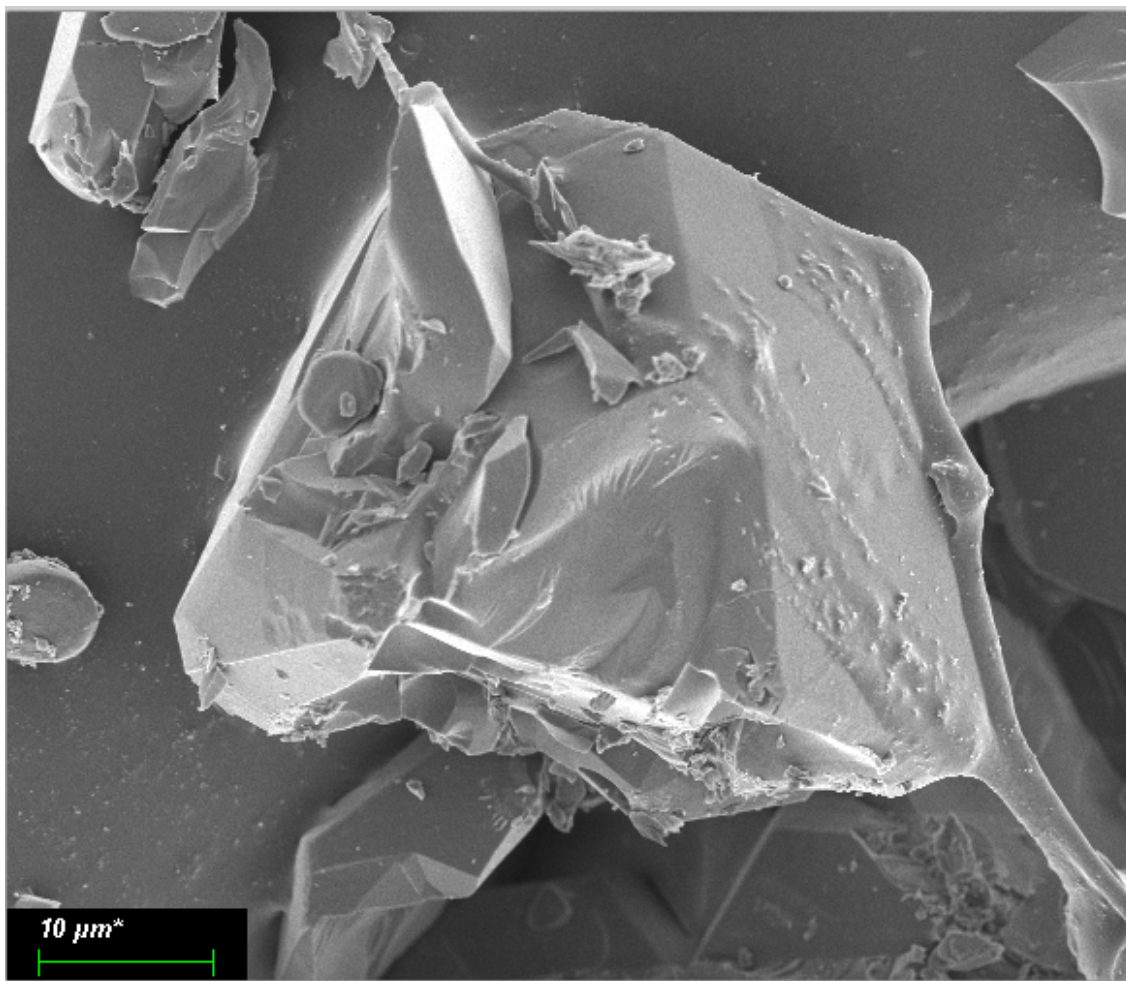


Figure 7.3: SEM image of the crystalline ZIF-62(Co) sample.

The SEM images of the melt-quenched ZIF-62(Co) in fig. (7.4) show the characteristic octahedral shape, including some of the expected imperfections. The high viscosity of ZIF-62(Co) prevents the crystals from collapsing completely, as the particles have maintained their shape. The glassy nature of the sample can be noticed by the formation of cracks that originate on flat sides of the surfaces of each particle, something that is not characteristic of crystalline ZIF-62(Co) particles, and are very unlikely to have formed due to an external force.

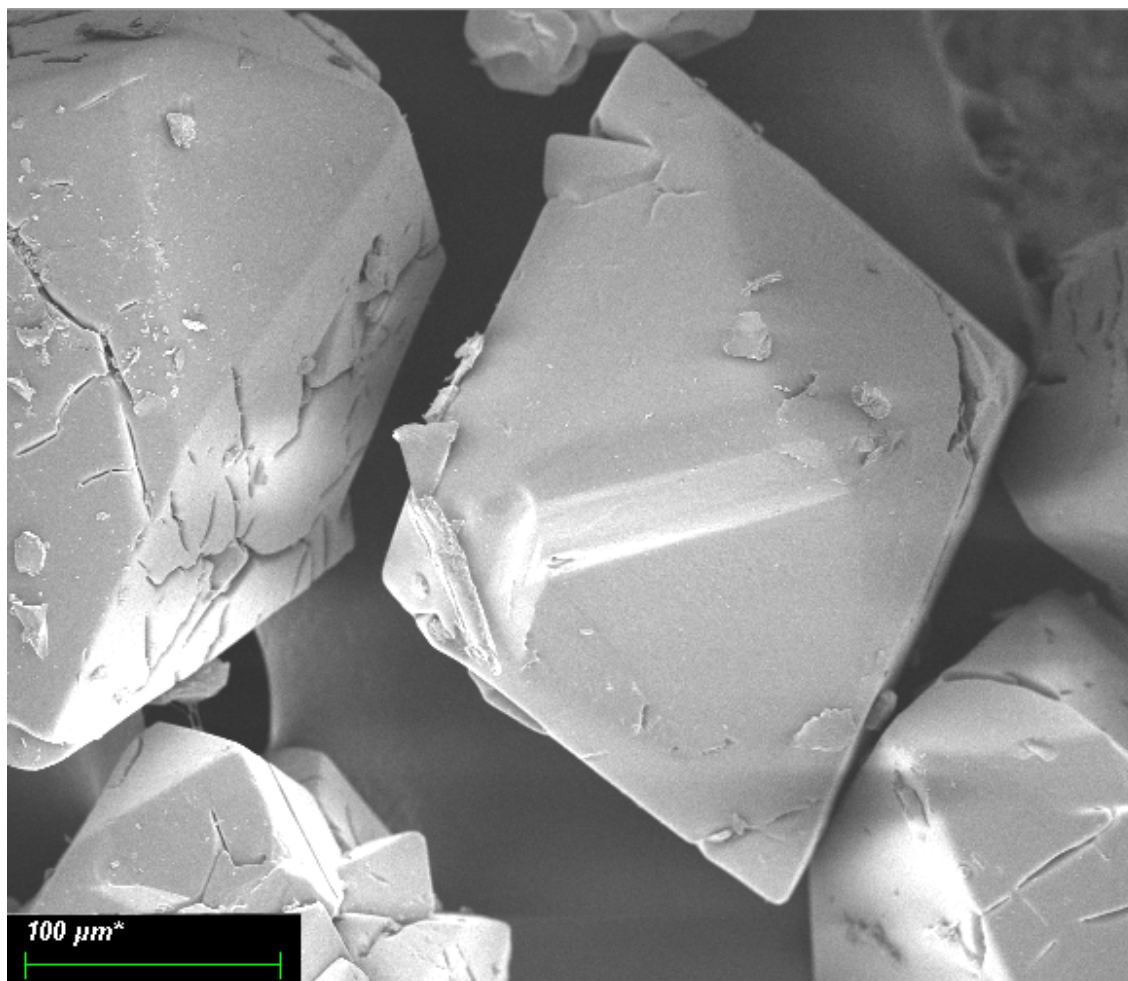


Figure 7.4: SEM image of the melt-quenched ZIF-62(Co) sample.

7.3 Proton-NMR

The linker composition of ZIF-62(Co) was determined using liquid ^1H -NMR using a 5:1 DMSO and DCl solution, where the DCl is able to dissolve the ZIF into its separate components. The relative areas of the signal for the hydrogen at position 2 in both Im and bIm were compared to find the estimate the ratio of the linkers. The signal for the hydrogen at this position is different, due to a slightly stronger deshielding in bIm, resulting in a difference in the frequency of the signal.

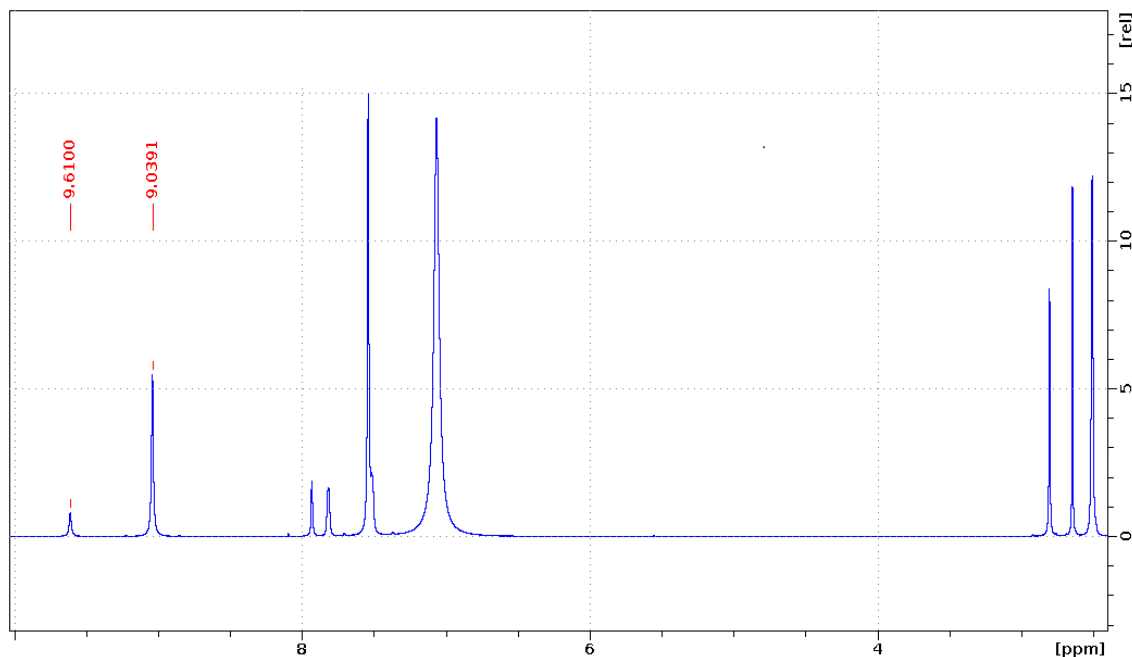


Figure 7.5: Spectra of ZIF-62(Co) dissolved in a 5:1 DMSO to DCl solution. The assigned peaks belong to the hydrogen atoms at the 2-position in Im and bIm respectively.

The weaker signal in figure 7.5 at 9.6100 ppm is for bIm, and the stronger signal at 9.0391 ppm is for Im. Converting the integrals to the ratio common in the empiric formula of ZIFs results in the composition $\text{Co}(\text{Im}_{1.70}\text{bIm}_{0.30})$, which has a greater bIm content than the expected ZIF-62 with the composition $\text{Zn}(\text{Im}_{1.75}\text{bIm}_{0.25})$. This is similar to previous estimations of the ratio specifically for ZIF-62(Co) using ^1H -NMR [65].

7.4 X-ray Photoelectron Spectroscopy

XPS was used to determine significant changes in the chemical bonding during the second cycle (after the initial SEI formation). All the XPS spectra are for crystalline ZIF-62(Co) and were taken at different potentials seen in fig. 7.9.

The release of 2p electrons from Co was measured, and from a quick glance at fig. (7.6) it can be seen that there are satellite features. These are characteristic of Co^{2+} and are located at the binding energies of 786 eV, 797 eV and 802 eV [69]. These features are present at both the cell potential of 0V and 3V, which is the entire voltage range during cycling. There is also no sign of metallic Co, which is expected to have a sharp peak starting at 778 eV and ending at 780 eV [70]. This indicates that there is no reduction in the regular oxidation state of Co(II) in crystalline ZIF-62(Co) during the cycling process.

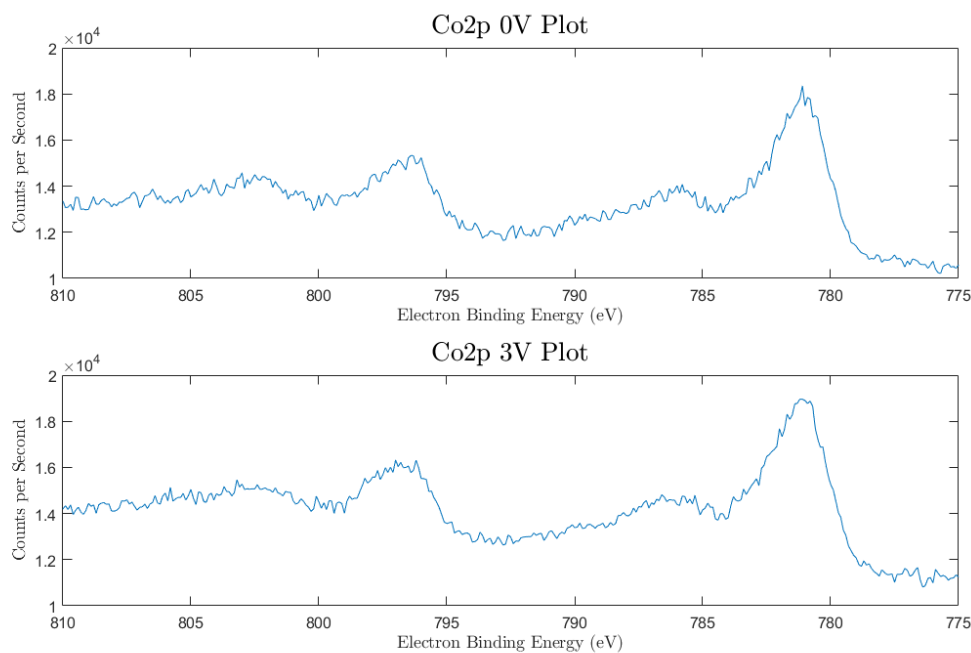


Figure 7.6: (Top) XPS scan of the Cobalt region when the cell is at 0V. (Bottom) Similar scan but performed at a cell potential of 3V.

Repeating the same for the 1s electrons from carbon, shows no changes either. The main peak in fig. (7.7) in the range of 281-287 eV consists of the carbon-carbon signature at 284 eV and carbon-nitrogen signature causing the asymmetrical slope at 286 eV [71]. These are expected signatures from the imidazole linkers and carbon black additive. The small satellite peak at 291 eV is assigned to $\pi-\pi$ interactions between the imidazole linkers, also commonly seen in other materials with similar interactions.

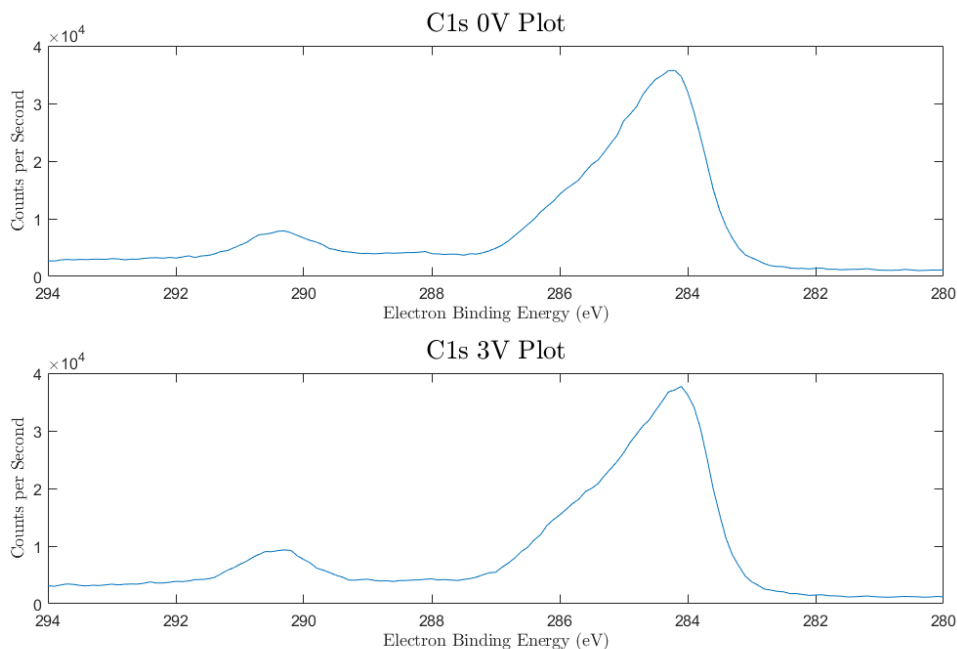


Figure 7.7: (Top) XPS scan of the Carbon region when the cell is at 0V. (Bottom) Similar scan but performed at a cell potential of 3V.

The 1s electrons from nitrogen only show a single unchanging peak in fig. (7.8) at 399 eV, which is an expected value for aromatic nitrogen-carbon bonds [72]. The linkers are the only source of nitrogen, and the two nitrogen atoms in imidazole and benzimidazole have the same chemical environment.

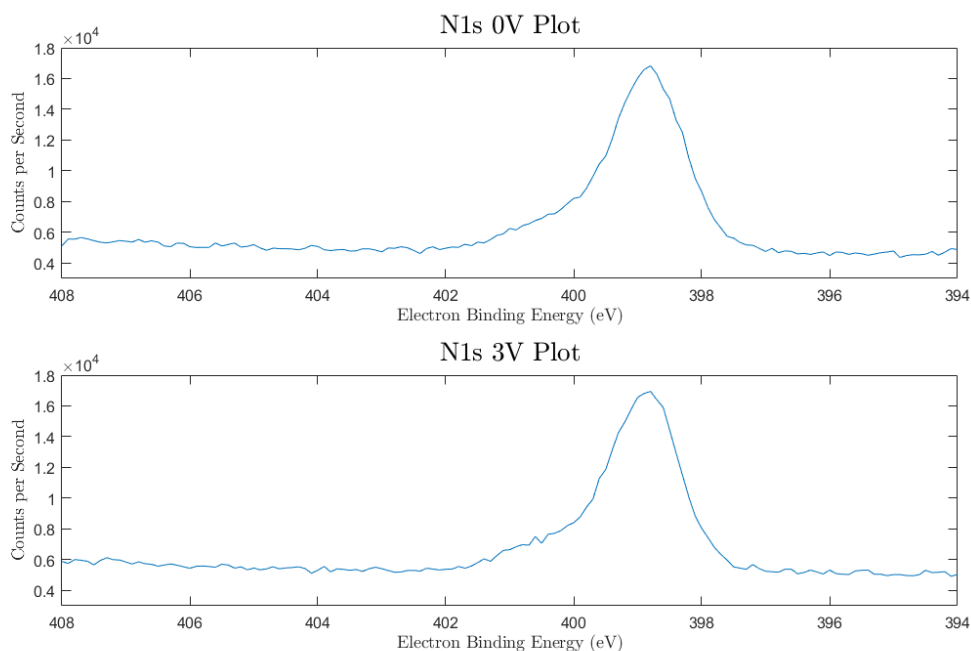


Figure 7.8: (Top) XPS scan of the Nitrogen region when the cell is at 0V. (Bottom) Similar scan but performed at a cell potential of 3V.

Comparing all the scans in fig. (7.9) shows that no change occurred from start to finish of the second cycle. Overlapping of the signals makes it more clear, that the signatures remains the same even with some variations in number of measured electrons.

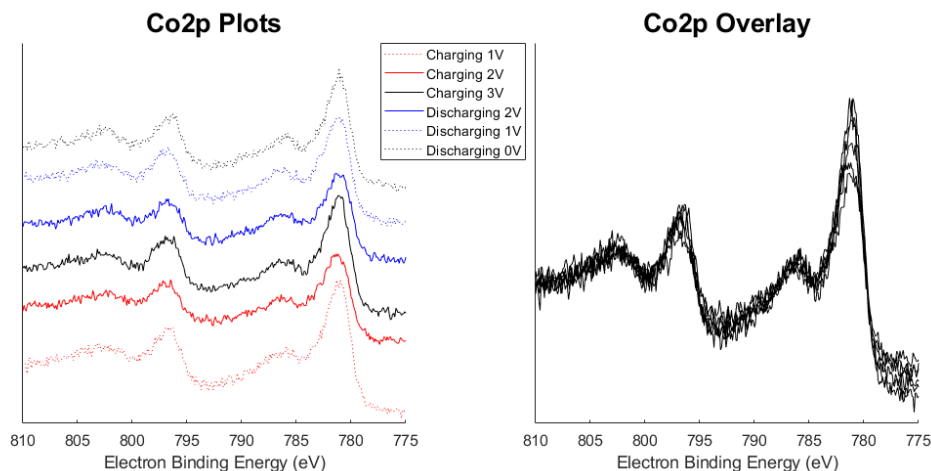


Figure 7.9: (Left) XPS scans in the Cobalt region for different cell potentials. (Right) All the scans placed on top of each other.

The lack of any changes in the binding energies of the electrons indicates that the lithiation process does not significantly change the bonding and oxidation state of the ZIF-62(Co) active material. This makes it likely that the storage of Li ions occurs by an intercalation mechanism without covalent bonding.

7.5 Differential Scanning Calorimetry

DSC is used to identify thermodynamic events that occur during heating. Fig. (7.10) shows the behaviour of crystalline ZIF-62(Co) during heating. The DMF solvent used in solvothermal synthesis is removed from the pores with an endothermic evaporation event. The melting process for a 10 mg sample at a 10 K/min heating rate has an onset at 390 $^{\circ}C$ and has completely finished at 430 $^{\circ}C$. During melt-quenching of a larger sample the process takes longer to reach thermal equilibrium, but the melting point T_m can be considered as the end of the peak at 430 $^{\circ}C$. Decomposition of the ZIF-62(Co) becomes significant at 490 $^{\circ}C$ and likely already occurs to some degree at lower temperatures if the heating rate was lower than 10 K/min .

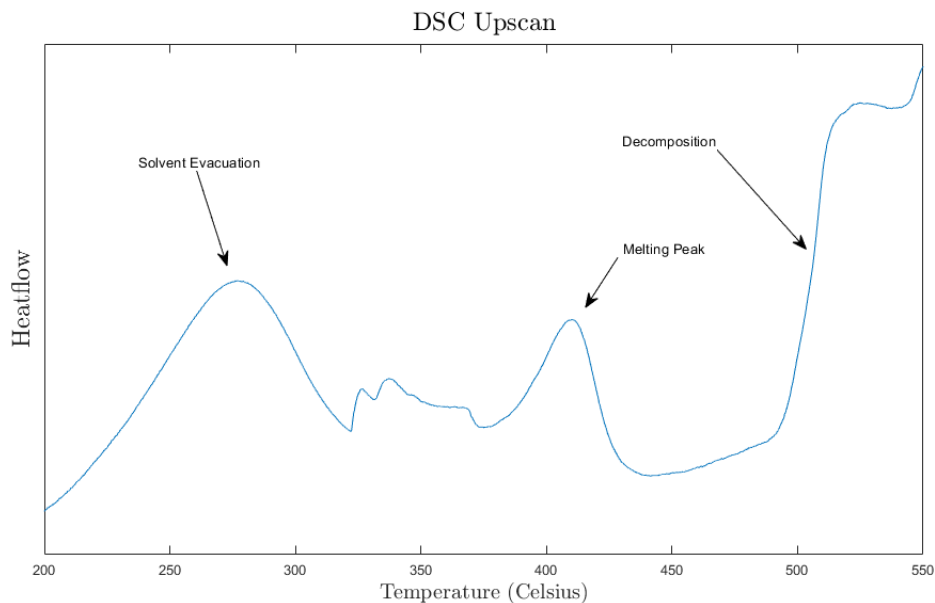


Figure 7.10: Heating curve of ZIF-62(Co). Evacuation of solvent, melting and decomposition assigned to the three main endothermic events.

Fig. (7.11) is a reheating upscan of crystalline ZIF-62(Co) after the being melt-quenched in the DSC crucible by an initial heating and cooling cycle at 10 K/min . The evacuation and melting process do not occur, as the solvent has already been evacuated during the initial heating, and the melting process does not occur in glassy materials. The glass transition peak confirms the glassy nature of the melt-quenched ZIF-62(Co). The glass transition occurs over a fairly broad temperature range of $320\text{--}370\text{ }^\circ\text{C}$ and only has a small increase in heat capacity of $\Delta C_p \approx 0.08\text{ J/(mol K)}$ (+6%), both characteristic of glass with a low liquid fragility index m . The glass transition is determined to be at $330\text{ }^\circ\text{C}$ indicated by the vertical line, marking the intersection between the projected C_p and the tangent of the inflection point of the glass transition step. The T_m/T_g ratio for ZIF-62(Co) is 0.85, which deviates from the general rule of thumb for glass formers at $T_m/T_g \approx 0.67$ [73]. The higher ratio means that it is easier to vitrify ZIF-62(Co) than most other glass formers.

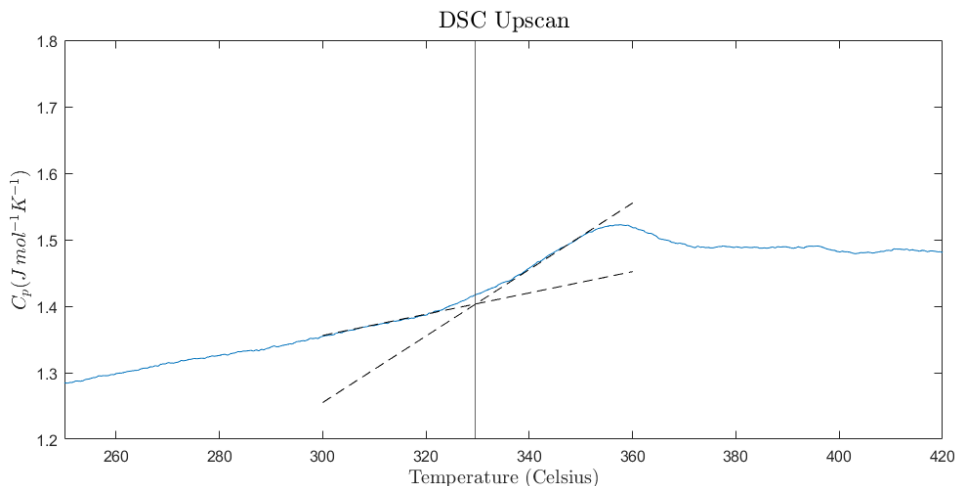


Figure 7.11: Plot of the temperature vs. the isobaric heat capacity. The step in the heat capacity is the second order glass transition, only seen in glassy materials where there is no solid-liquid first order transition.

These results tell us something about the structural changes that ZIF-62(Co) undergoes during melt-quenching. During melt-quenching ZIF-62(Co) is treated at higher temperatures than it usually would, which could lead to differences in cell performance between crystalline and glassy ZIF-62(Co). One difference could be a decrease in charge-transfer resistance as less of the pore volume is occupied by the solvents used during solvo-thermal synthesis. Some decomposition that occurs during the melt-quenching can also further increase the porosity, as a small percentage of the linkers are destroyed by pyrolysis.

The high T_m/T_g ratio and the weak glass transition indicate that the structural difference between the glassy and the liquid state are small. This is further backed up by a low liquid fragility and high viscosity [65], as well as no noticeable differences in atomic pair distribution functions of ZIF-62 glass before and after annealing [34]. The case can be made that the short range order does not change due to the strength of the bonds, even after melting. The increased density [65] and low Gibbs energy of crystallisation [34] of ZIF-62 further indicate that the glassy state is achieved due to an inability for the Co nodes and imidazole linkers to rearrange back into the zeolite crystalline structure.

Whether the amorphous long range disorder is beneficial in regards to the electrochemical performance can only be determined by galvanostatic charge-discharge tests. It is not always certain that the percolation channels in glassy materials improve diffusion over highly ordered crystalline structures, especially in the case of ZIFs that have a large pore volume.

7.6 Cyclic Voltammetry

CV curves were obtained for the three initial charge-discharge cycles of the cells. The three cells that were tested are ZIF-62(Co) glass (annealed), ZIF-67 and ZIF-67 ball-milled. Positive current values are the result of oxidation and the release of electrons when the applied potential is increased (delithiation). Negative current values are the

result of reduction when the applied potential is decreased (lithiation).

Fig. (7.12) shows typical behaviour with an active first cycle, followed by less active and more consistent second and third cycles. The main oxidation peak is at 1.3V, although the current is fairly consistent from 0.4V to 1.6V. Reduction does not occur until a potential of 1.2V and steadily increases. There is a peak at 0.6V followed by an increase in reduction below 0.4V.

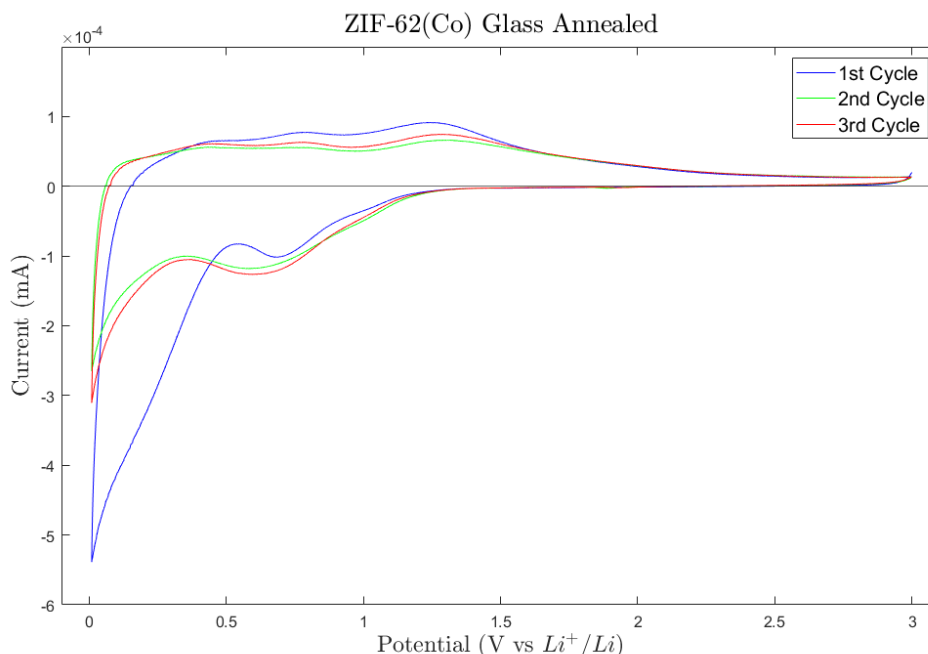


Figure 7.12: The applied potential plotted vs. the resulting current for glassy ZIF-62(Co). The potential is first reduced to 0V (initial lithiation) and then increased back to 3V (subsequent delithiation).

Fig. (7.13) and (7.14) have a steady delithiation process with a small peak at 1.2V, followed by a lithiation process with a lot of noise. There seems to be similarities between the peaks of the crystalline and ball-milled ZIF-67 during the first lithiation scan at 1.6V, 1.3V, 0.7V and 0.6V. However, without a galvanostatic charge-discharge measurement to see the CE during the initial cycle, it would be difficult to know whether it is related to SEI formation or a more specific side-reaction that occurs in ZIF-67. Following cycles do not show the same peaks during the lithiation process. There is almost no difference between the crystalline and the ball-milled ZIF-67, indicating the the mechanism of lithiation and delithiation remains the same after inducing structural defects through milling.

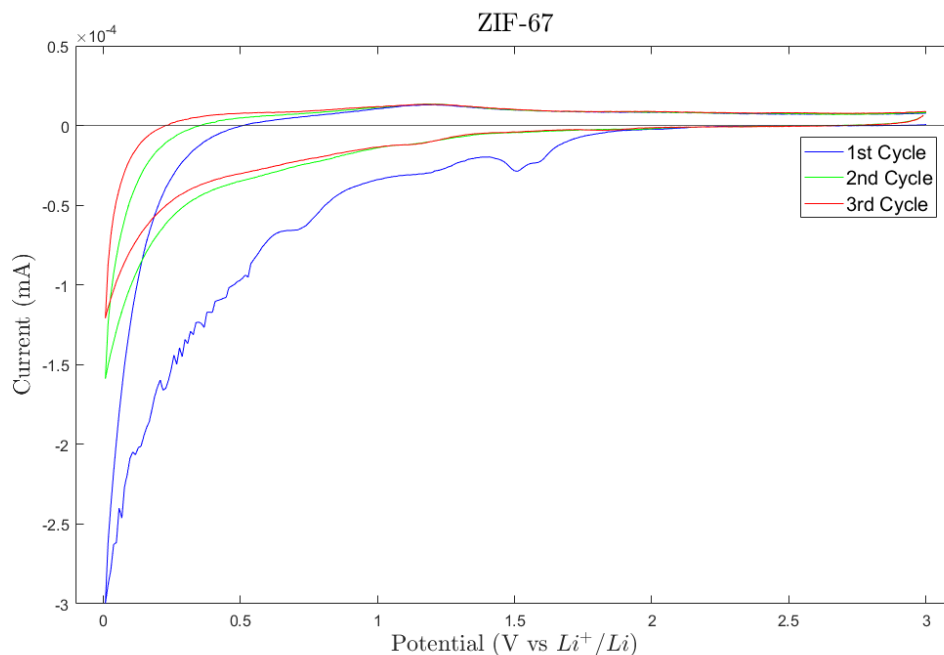


Figure 7.13: The applied potential plotted vs. the resulting current for ZIF-67. The potential is first reduced to 0V (initial lithiation) and then increased back to 3V (subsequent delithiation).

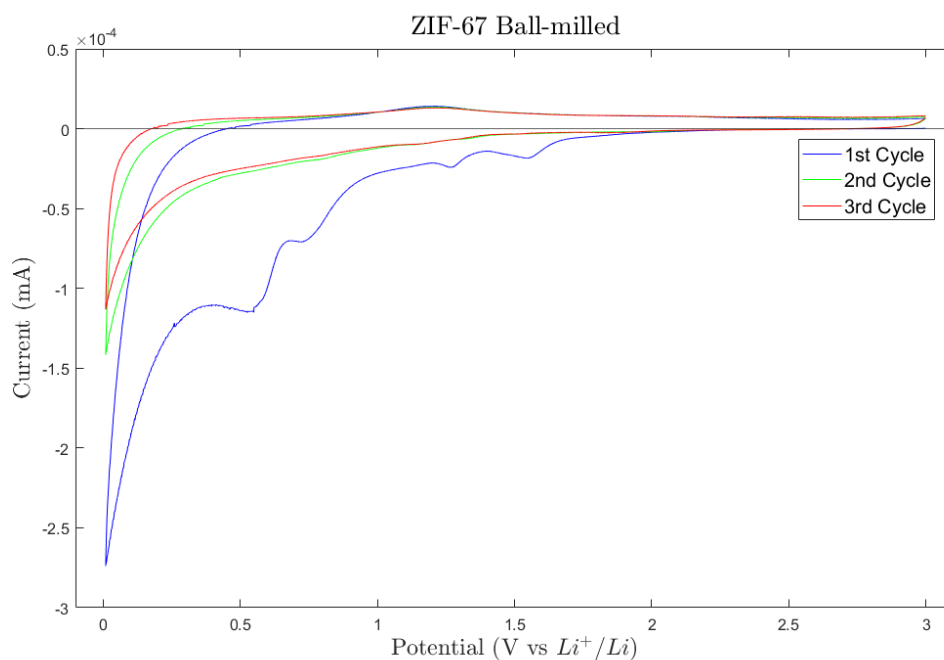


Figure 7.14: The applied potential plotted vs. the resulting current for ball-milled ZIF-67. The potential is first reduced to 0V (initial lithiation) and then increased back to 3V (subsequent delithiation).

The oxidation current remaining at higher potentials and the lack of sharp peaks during the second and third cycles indicates that the potential curve of the OCV will be S-shaped, and the average anode potential will be lower than that of graphite based anodes. This aligns with structural stability of the XPS results. No structural change means that the

potential will gradually decrease in electrode potential and no plateau will be observed.

7.7 Galvanostatic Charge-Discharge Cycling

Data for the same three samples as for the CV curves was received (ZIF-62(Co) glass (annealed), ZIF-67 and ZIF-67 ball-milled).

Fig. (7.15) shows the evolution of the specific capacity of ZIF-62(Co) glass (annealed) for a total of 741 charge-discharge cycles performed at an applied current of 1 A/g in the voltage range of 0-3V vs Li⁺/Li. The initial capacity is 584 mAh/g and drops to 246 mAh/g on the second cycle. The CE of the first cycle is 36%. The decline in capacity slows down until a minimum capacity of 120 mAh/g is reached at cycle 31. At this cycle the CE has become stable and remains between 98-100%. A slow increase in the capacity continues, followed by a slowing down of the improvement until a new maximum capacity of 540 mAh/g is reached at cycle 723 (92% of the initial and 4.5 times more than the lowest). This value is considered the maximum the capacity can recover, before the capacity will decline. This is not confirmed from this graph, however, the trajectory slowing down combined with an average CE of 99.3% (99.5% when ignoring the initial low CE values) will eventually result in a decline of the capacity.

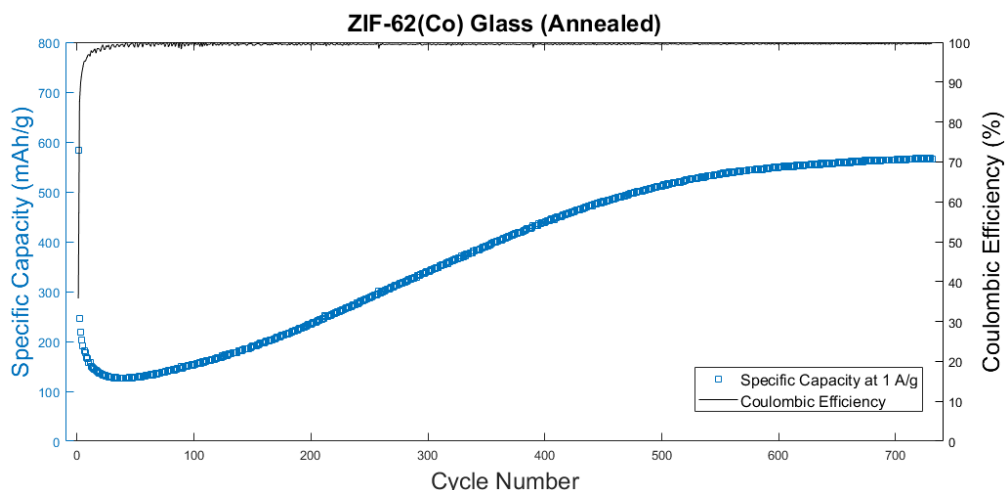


Figure 7.15: Cycling performance and coulombic efficiency for ZIF-62(Co) glass (annealed) with a current density of 1 A/g.

Fig. (7.16) shows the evolution of the specific capacity for crystalline ZIF-67 for a total of 813 cycles with the parameters for current and voltage being the same as the previous. The initial capacity is 282 mAh/g and drops to 86 mAh/g on the second cycle. The CE of the first cycle is 22%. The decrease slows down and reaches a minimum of 66 mAh/g at cycle 12. The maximum capacity before the cycling ended was 197 mAh/g at cycle 812 (70% of the initial and 3 times more than the lowest). The CE remains below 98% until cycle 70, and remains at 98-99%. The average CE is 98.4% with the highest single CE value at 99.7%, never reaching 100%. From the trajectory it seems that more of the capacity could have recovered if the cycling had continued.

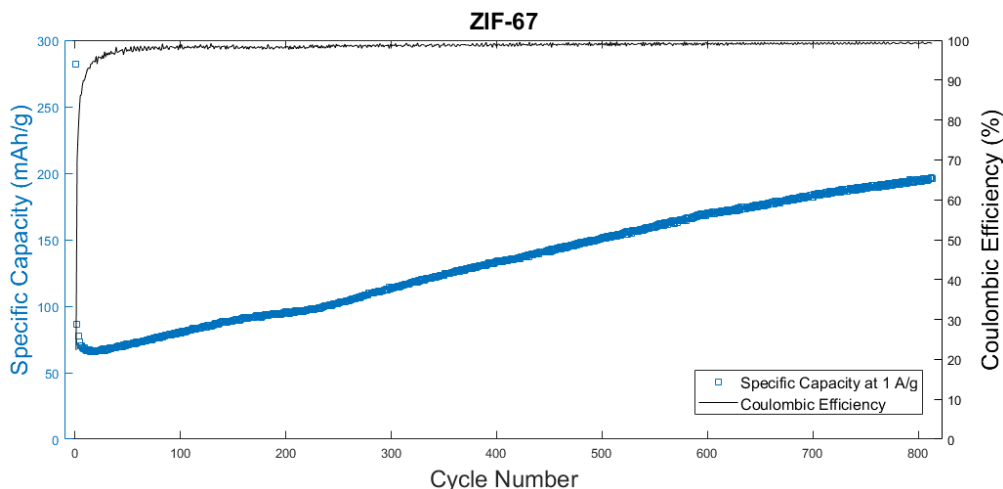


Figure 7.16: Cycling performance and coulombic efficiency for ZIF-67 with a current density of 1 A/g.

Fig. (7.17) shows the evolution of the specific capacity for crystalline ZIF-67 for a total of 1000 cycles. The first few capacity measurements are inconsistent, which means that no accurate estimate for the initial capacity can be given. Similarly the CE is inaccurate in this region. The rest of the curve looks similar to the glassy ZIF-62(Co) with a capacity closer to that of the ZIF-67 crystal. The lowest capacity (aside from the first few measurements) is 74 mAh/g at cycle 39. The capacity increases to 327 mAh/g at cycle 781 (4.4 times more than the lowest). The CE stabilises at cycle 60 where it remains between 98-100% with an average of 99.5% for cycles 60 to 1000. The decrease in capacity can be seen during the last 180 cycles, with a total decrease of 14 mAh/g over the 180 cycles. This decrease is equivalent to an CE of 99.98% if we go by eq. (2.5), and does not match the measured average CE of 99.5%. This could mean that more capacity is recovered while simultaneous degradation decreases the resulting capacity, or that the equation is not accurate for the degradation process in ZIF-67.

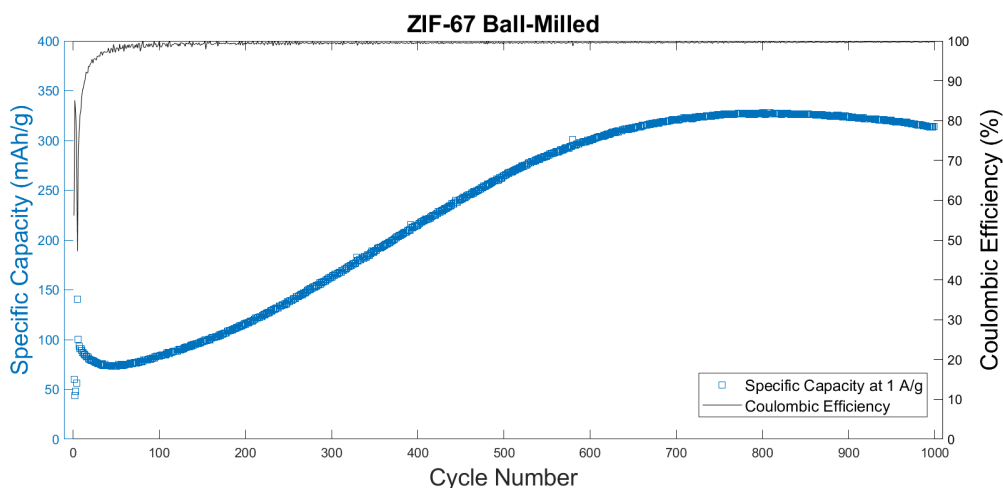


Figure 7.17: Cycling performance and coulombic efficiency for ball-milled ZIF-67 with a current density of 1 A/g.

There was seen some variation in the specific capacity based on cell assembly in the

range of 0-40 mAh/g , with the lower variation belonging to the ZIF-67 samples. Tests at a current of 500 and 100 mA/g were performed, but showed no improvement in the capacity or the CE in the first 100 cycles, and did not fully recover their capacity before the cycling test had concluded. The gradient of their capacity recovery was not greater than at 1 A/g , although the ultimate decline in capacity could maybe be delayed by the lower applied currents, based on the stability of other materials that remain stable or recover some capacity [cite].

The lower initial specific capacity of ZIF-67 was expected, due to the difference in the density of the porous crystalline ZIF-67 and the dense annealed glassy ZIF-62(Co). The shape of the capacity curve seems to be related to the CE, where a smoother curve is seen for the two samples where the average CE was higher. This could mean that the capacity recovery is not related to the number of cycles, but the rate at which it is recovered. The ZIF-62(Co) glass and the ball-milled ZIF-67 both show faster recovery, but eventually reach a maximum followed by a decline. The crystalline ZIF-67 maintains its trajectory longer when comparing it with the ball-milled sample at the same number of cycles.

This could hint towards an order-disorder-collapse transition, where the melt-quenching and ball-milling make the first step from order to disorder easier than for the crystalline structure. The downside is that it also results in faster collapse of the structure

Figures (??) show the potential curves for charging and discharging related to the cycling data. The curves for the lowest capacity, highest capacity and the three initial measurements are included. Note that the three initial curves for ZIF-67 ball-milled in fig. 7.20 are related to data that could be inaccurate, as it corresponds to first three points in fig. 7.17.

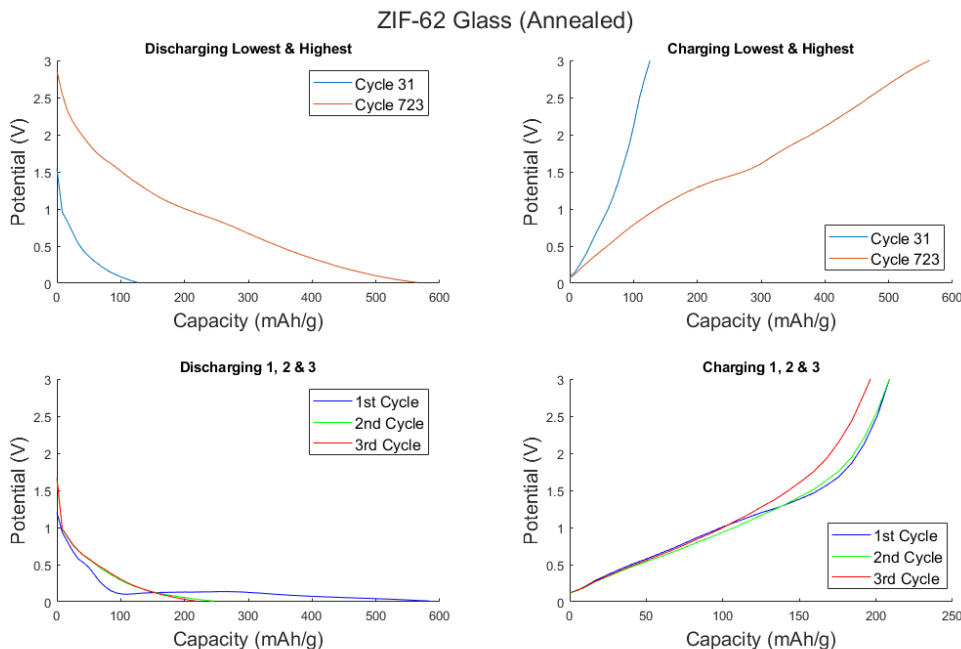


Figure 7.18: (Left) Discharging (lithiation) potential curves at 1 A/g . (Right) Charging (delithiation) potential curves at 1 A/g . The specific cycles are chosen for the highest and lowest specific capacity.

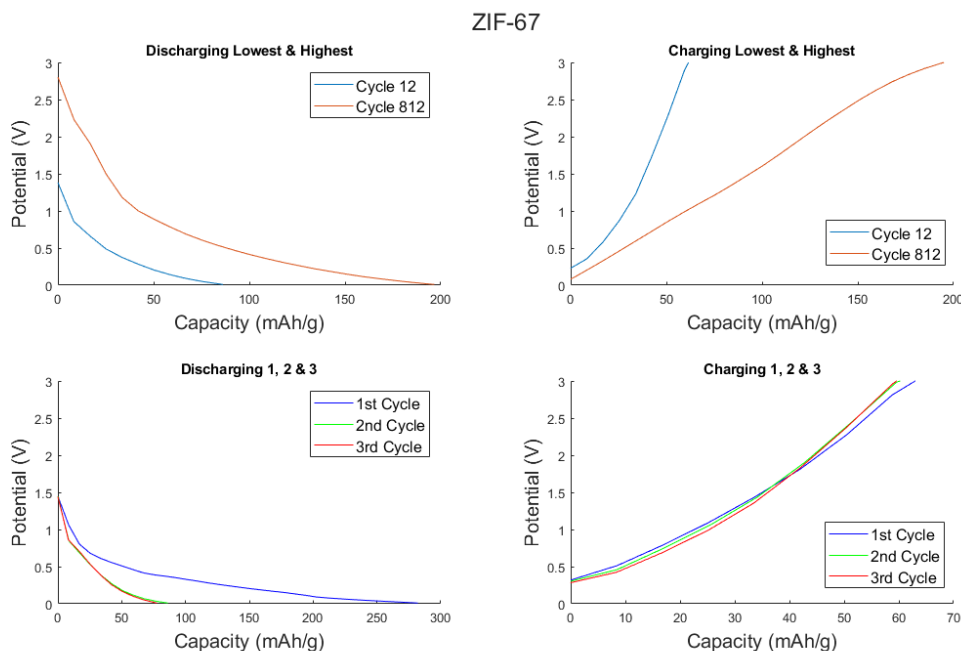


Figure 7.19: (Left) Discharging (lithiation) potential curves at 1 A/g. (Right) Charging (delithiation) potential curves at 1 A/g. The specific cycles are chosen for the highest and lowest specific capacity.

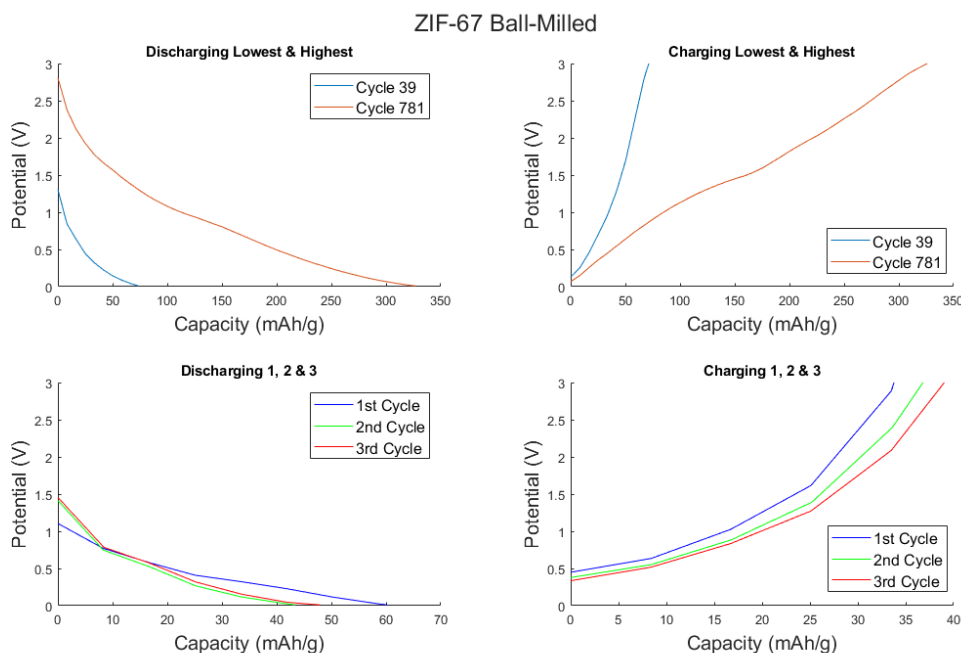


Figure 7.20: (Left) Discharging (lithiation) potential curves at 1 A/g. (Right) Charging (delithiation) potential curves at 1 A/g. The specific cycles are chosen for the highest and lowest specific capacity.

The potential curves for the three initial measurements show an expected result, where the first discharge shows a high capacity followed by a low capacity for the first discharge, indicating an initial irreversible capacity. The second and third cycle overlap nicely, similar to the CV curves. All the samples show an increase in the average potential as the capacity

increases. The shape of potential curves show that there is no potential plateau, but there is a change in the potential gradient during discharging of the cell

7.8 Electrochemical Impedance Spectroscopy

Two sets of EIS data were received for three samples (ZIF-62(Co) glass (annealed), ZIF-67 and ZIF-67 Ball-milled). The EIS measurements were performed before the long-term cycling experiment, so the structure of the active material should not have undergone any changes due to cycling.

The values derived from the EIS data are summed up in table (7.1). The difference in electrolyte resistance Z_e is difficult to attribute directly to the different types of active material, the differences are small enough to be measurement errors or remnants from slight variations in cell assembly, but, should stem from shorter diffusion paths towards the electrode surface. The difference in charge transfer resistance Z_{ct} between the crystalline and ball-milled ZIF-67 is expected from the difference in particle size surface defects after the ball-milling. Less expected is the difference in the value of σ , which is inversely proportional with the Li ion diffusion. A physical explanation could be the formation of shorter paths for Li ion diffusion in the ball-milled ZIF-67, compared to the crystalline ZIF-67.

Table 7.1: An overview of the EIS related values for the three samples.

Sample	$Z_e(\Omega)$	$Z_{ct}(\Omega)$	$C(\mu F)$	$\sigma(\Omega s^{-1/2})$
ZIF-62(Co) Glass (Annealed)	1	65	3.5	108
ZIF-67	1	250	5.1	467
ZIF-67 Ball-milled	3	87	3.2	120

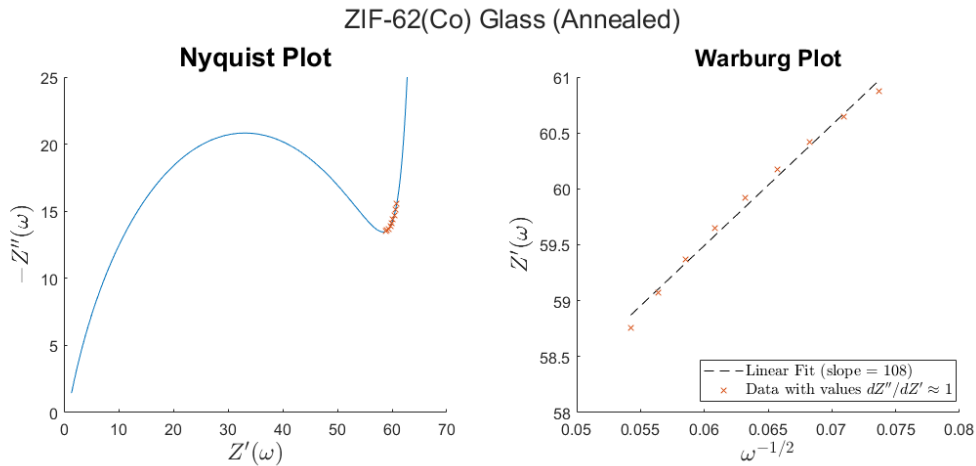


Figure 7.21: (Left) Nyquist plot of the real and imaginary impedance. (Right) A linear fit for the real impedance that resides in the Warburg region of the Nyquist plot and the reciprocal squareroot of the angular frequency. Red crosses are the same points in both plots.

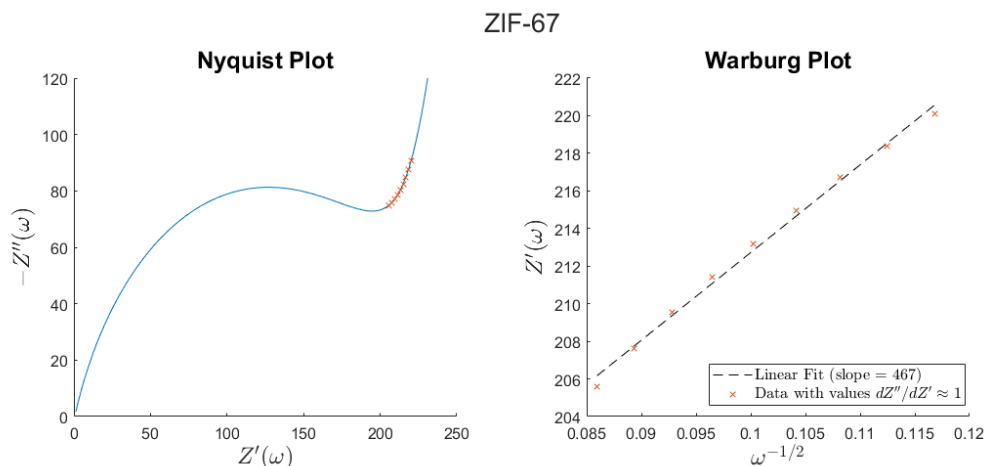


Figure 7.22: (Left) Nyquist plot of the real and imaginary impedance. (Right) A linear fit for the real impedance that resides in the Warburg region of the Nyquist plot and the reciprocal squareroot of the angular frequency. Red crosses are the same points in both plots.

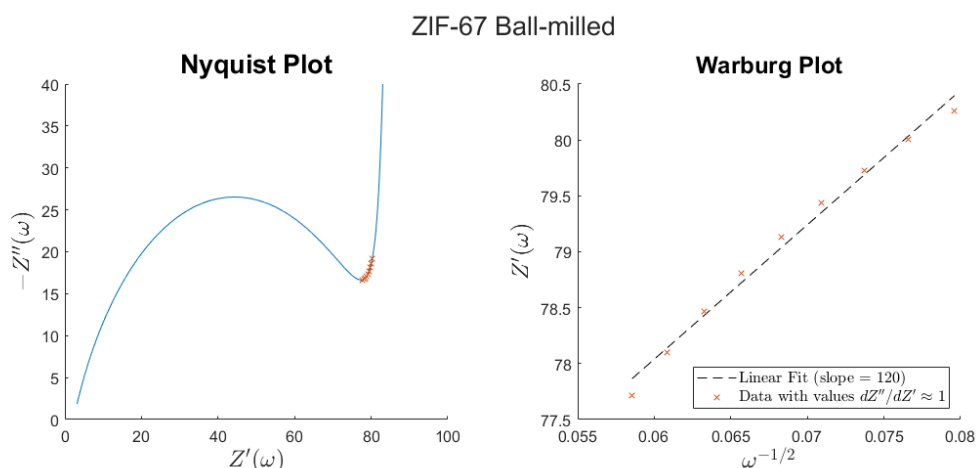


Figure 7.23: (Left) Nyquist plot of the real and imaginary impedance. (Right) A linear fit for the real impedance that resides in the Warburg region of the Nyquist plot and the reciprocal squareroot of the angular frequency. Red crosses are the same points in both plots.

7.9 BET Surface Area

Data for the BET (N_2 adsorption at $T = 77K$) surface area for crystalline ZIF-67 was obtained at $1252 \text{ m}^2/\text{g}$. The extrapolated average pore diameter was determined to be 1.59 nm. These values are greater than that of ZIF-8, and close to previously reported values for ZIF-67 at $1204 \text{ m}^2/\text{g}$ [54].

7.10 Fourier Transformed-Infrared Transmittance Spectroscopy

FT-IR was performed on crystalline ZIF-62(Co), ZIF-62(Co) glass and glass that was annealed for 24 hours. The purpose was to see the effect annealing has on interaction

between the Co nodes and the linkers. The wavenumbers are related to the resonance energy of the stretching and various swinging modes of the bonds. The energy bands for the Co-N bonds have a shorter wavenumber than the bonds between carbon and nitrogen. The topleft graph in fig. 7.24 depicts the entire mid-range infrared signature of crystalline ZIF-62(Co). Top right and bottom left focus on the bands in the 400-500 cm^{-1} region. The glassy ZIF-62(Co) shows broadening of the peaks and a small shift towards lower wavenumbers for both peaks. Bottom right shows the crystalline and glassy sample, and the third 24 hour annealed sample. The annealed sample experienced decomposition, so might not be representative of what should ideally happen. The vertical line shows that there is a redshift in the wavenumber from crystal to glass.

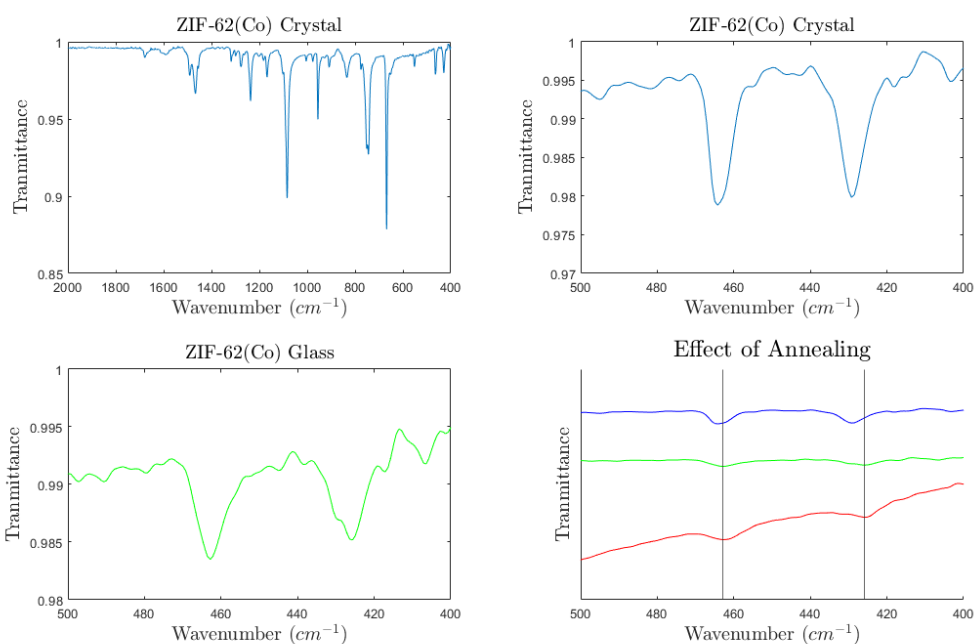


Figure 7.24: (Top Left) FT-IR transmittance spectrum for ZIF-62(Co) in region 400-2000 cm^{-1} . (Topright) Closer look at the two peaks close to the near IR region for Zif-62(Co). (Bottom Left)

The shift towards slightly lower wavenumbers indicates a small change in the bonding of ZIF-62(Co) after melt-quenching.

7.11 Discussion

Understanding the effect of annealing will not be possible since I was unable to obtain data of the electrochemical tests before handing in the thesis. Therefore the focus of this discussion will focus more on the general aspects of ZIF active materials and the difference between the crystalline and ball-milled ZIF-67.

XPS and the cell potential curves from galvanostatic cycling indicate that there is no change in the chemical composition of the active material during charging and discharging. This strengthens the general assumptions that the lithiation process in MOFs is intercalation by *pi*-cation interactions between the aromatic quadrupole and the Li ions,

and potentially the electrostatic interactions between the nitrogen in the imidazole linker and the Li ions [11].

There is likely a connection between the charge-transfer resistance from the EIS data and the rate at which the capacity is recovered. The lower resistance for electrochemical processes in the active material speeds up the mechanism that is related to the increase in capacity. It hints towards a order-disorder process that changes the structure of the active material as it is cycled. Amorphous materials already have a degree of disorder, which decrease the electrochemical work required to change the structure. Crystalline ZIF-67 had the highest charge-transfer resistance and Warburg impedance, combined with a lower CE and slower recovery of the capacity. These points are congruent with the concept of a order-disorder transition, where the ordered crystal is more difficult to turn amorphous through electrochemical processes.

The ZIF-62(Co) glass likely had a higher capacity than ZIF-67 due to the higher density, although it is not clear how exactly difference in the imidazolate linkers would change the capacity. The electrochemical data for the crystalline ZIF-62(Co) and the non-annealed ZIF-62(Co) glass would have to be collected and compared to get a clearer picture.

7.12 Conclusion

The electrochemical performance of ZIF-62(Co) glass that was annealed for 2 hours, ZIF-67 and ball-milled ZIF-67 was determined. All samples showed an initial decrease in the specific capacity, followed by a slow increase in the capacity over the course of 700 or charge-discharge more cycles. Ball-milling showed an significant changes to the electrochemical performance of ZIF-67. Further conclusions regarding ZIF-62(Co) are left unsaid until more data is collected.

Bibliography

- [1] M. Wakihara C. Iwakura S. Kohjiya I. Tanaka T. Minami, M. Tatsumisago. *Solid State Ionics for Batteries*. Springer, 2001.
- [2] European Environment Agency. *Electric vehicles from life cycle and circular economy perspectives (TERM 2018 : Transport and Environment Reporting Mechanism (TERM) report)*. European Environment Agency, 2018.
- [3] Kaveh Mazloomi and Chandima Gomes. Hydrogen as an energy carrier: Prospects and challenges. *Renewable and Sustainable Energy Reviews*, 16, 2012.
- [4] Jerald A. Caton. The thermodynamics of internal combustion engines: Examples of insights. *Inventions*, 33, 2018.
- [5] T. Hofman and C.H. Dai. *Energy efficiency analysis and comparison of transmission technologies for an electric vehicle*. 2010 IEEE Vehicle Power and Propulsion Conference, 2010.
- [6] A. El Kharbachi et al. Exploits, advances and challenges benefiting beyond li-ion battery technologies. *Journal of Alloys and Compounds*, 817, 2020.
- [7] Gene Berdichevsky. *The Future of Energy Storage*. Sila Nanotechnologies, 2020.
- [8] Hiroyasu Furukawa, Kyle E Cordova, Michael O’Keeffe, and Omar M Yaghi. The chemistry and applications of metal-organic frameworks. *Science (New York, N.Y.)*, 341(6149):1230444, aug 2013. doi: 10.1126/science.1230444.
- [9] Antje Henschel, Kristina Gedrich, Ralph Kraehnert, and Stefan Kaskel. Catalytic properties of MIL-101. *Chemical Communications*, (35):4192–4194, 2008. doi: 10.1039/b718371b.
- [10] Liang Chen et al. An exceptionally stable functionalized metal–organic framework for lithium storage. *Chemical Communications*, 51, 2015.
- [11] Ji Ping Zhu et al. The application of metal-organic frameworks in electrode materials for lithium–ion and lithium–sulfur batteries. *R. Soc. open sci.*, 6, 2020.
- [12] Jung-Ki Park. *Principle and Applications of Lithium Secondary Batteries*. John Wiley Sons, 2012.
- [13] Sandeep Bhattacharya et al. Effect of li2co3 deposition on electrochemical cycling-induced graphite damage. *ECS Transactions*, 35, 2011.
- [14] Sandeep Bhattacharya et al. Effect of li2co3 deposition on electrochemical cycling-induced graphite damage. *ECS Transactions*, 35, 2011.

-
- [15] Chaofeng Liu et al. Understanding electrochemical potentials of cathode materials in rechargeable batteries. *Materials Today*, 19, 2016.
- [16] Seiji Kumagai et al. Electrochemical impedance spectroscopy on the performance degradation of lifepo4/graphite lithium-ion battery due to charge-discharge cycling under different c-rates. *energies*, 12, 2019.
- [17] Laurence M. Peter. *Photoelectrochemistry: From Basic Principles to Photocatalysis*. Royal Society of Chemistry, 2016.
- [18] David Allart et al. Model of lithium intercalation into graphite by potentiometric analysis with equilibrium and entropy change curves of graphite electrode. *Journal of The Electrochemical Society*, 165, 2018.
- [19] Anton van der Ven et al. Understanding li diffusion in li-intercalation compounds. *Accounts of Chemical Research*, 46, 2013.
- [20] Weihong Qi et al. Gibbs free energy and size-temperature phase diagram of hafnium nanoparticles. *Journal of Physical Chemistry C*, 115, 2011.
- [21] Xue Yongqiang et al. Effect of particle size on electrode potential and thermodynamics of nanoparticles electrode in theory and experiment. *Electrochimica Acta*, 136, 2014.
- [22] Baichuan Sun and Amanda S. Bernard. The impact of size and shape distributions on the electron charge transfer properties of silver nanoparticles. *Nanoscale*, 9, 2017.
- [23] M. N. Obrovac and V. L. Chevrier. Alloy negative electrodes for li-ion batteries. *Chemical Reviews*, 114, 2014.
- [24] Ruiyuan Tian et al. Quantifying the factors limiting rate performance in battery electrodes. *Nature Communications*, 10, 2019.
- [25] Fangming Jiang and Peng Peng. Elucidating the performance limitations of lithium-ion batteries due to species and charge transport through five characteristic parameters. *Scientific Reports*, 6, 2016.
- [26] Christian Heubner et al. Diffusion-limited c-rate: A fundamental principle quantifying the intrinsic limits of li-ion batteries. *Advanced Energy Materials*, 10, 2020.
- [27] Yongchao Tang et al. Stabilized co³⁺/co⁴⁺ redox pair in in situ produced cose(2x)-derived cobalt oxides for alkaline zn batteries with 10000-cycle lifespan and 1.9-v voltage plateau. *Advanced Energy Materials*, 10, 2020.
- [28] John B. Goodenough and Kyu-Sung Park. The li-ion rechargeable battery: A perspective. *Journal of the American Chemical Society*, 135, 2013.
- [29] Jun Yang et al. *Advanced Nanomaterials for Electrochemical-Based Energy Conversion and Storage: Chapter 3 - Nanomaterials application in Li-Se and Na-Se batteries*. Elsevier, 2020.

- [30] Yimei Zhu et al. Chemical distribution and bonding of lithium in intercalated graphite: Identification with optimized electron energy loss spectroscopy. *American Chemical Society Nano*, 5, 2011.
- [31] Qi-Shi Du et al. The multiple roles of histidine in protein interactions. *Chemistry Central Journal*, 7, 2013.
- [32] Tor Grande et al. Van der waals density functional study of the energetics of alkali metal intercalation in graphite. *Royal Society of Chemistry Advances*, 4, 2014.
- [33] Chunyu Du et al. Understanding undesirable anode lithium plating issues in lithium-ion batteries. *Royal Society of Chemistry Advances*, 6, 2016.
- [34] Chao Zhou. Amorphization and glass formation of metal-organic frameworks. *Aalborg University*, 2018.
- [35] Cyrus Farivar. Federal regulators warn of risks to firefighters from electrical vehicle fires, 2021. URL <https://www.nbcnews.com/business/autos/federal-regulators-warn-risks-firefighters-electrical-vehicle-fires-n1271084>.
- [36] Robert A. Huggins. *Advanced Batteries: Materials Science Aspects*. Springer, 2009.
- [37] Nam-Soon Choi et al. Recent progress on polymeric binders for silicon anodes in lithium-ion batteries. *Journal of Electrochemical Science and Technology*, 6, 2015.
- [38] Xiuyun Zhao and Vesa-Pekka Lehto. Challenges and prospects of nanosized silicon anodes in lithium-ion batteries. *Nanotechnology*, 32, 2021.
- [39] Feixiang Wu and Gleb Yushin. Conversion cathodes for rechargeable lithium and lithium-ion batteries. *Energy Environmental Science*, 10, 2017.
- [40] Chengwei Gao et al. Optimized assembling of mof/sno2/graphene leads to superior anode for lithium ion batteries. *Nano Energy*, 74, 2020.
- [41] Rongli Jiang et al. Fe₃O₄ anodes for lithium batteries: Production techniques and general applications. *Comptes Rendus Chimie*, 22, 2019.
- [42] Vinodkumar Etacheri et al. Cobalt nanoparticles chemically bonded to porous carbon nanosheets: A stable high-capacity anode for fast-charging lithium-ion batteries. *ACS Applied Materials Interfaces*, 10, 2018.
- [43] Lee Loong Wong et al. Design of fast ion conducting cathode materials for grid-scale sodium-ion batteries. *Phys. Chem. Chem. Phys.*, 19, 2017.
- [44] Yaser Abu-Lebdeh et al. A high capacity silicon-graphite composite as anode for lithium-ion batteries using low content amorphous silicon and compatible binders. *Journal of Materials Chemistry A*, 1, 2013.
- [45] Eva Fox. Tesla silicon anode will be the key to next-level fast charging, 2020. URL <https://www.tesmanian.com/blogs/tesmanian-blog/tesla-silicon-fast-charge-is-on-the-way>.

- [46] Joaquin Silvestre-Albero et al. Molecular sieving properties of nanoporous mixed-linker zif-62: Associated structural changes upon gas adsorption application. *ACS Applied Nano Materials*, 4, 2021.
- [47] Yanshuo Li et al. A mof glass membrane for gas separation. *Angewandte Chemie*, 132, 2020.
- [48] Neng Li et al. Unraveling the effects of linker substitution on structural, electronic and optical properties of amorphous zeolitic imidazolate frameworks-62 (a-zif-62) glasses: a dft study. *RSC Advances*, 10, 2020.
- [49] Thomas D. Bennett, Yuanzheng Yue, Peng Li, Ang Qiao, Haizheng Tao, Neville G. Greaves, Tom Richards, Giulio I. Lampronti, Simon A.T. Redfern, Frédéric Blanc, Omar K. Farha, Joseph T. Hupp, Anthony K. Cheetham, and David A. Keen. Melt-Quenched Glasses of Metal-Organic Frameworks. *Journal of the American Chemical Society*, 138(10):3484–3492, mar 2016. doi: 10.1021/jacs.5b13220.
- [50] Wha-Seung Ahn et al. Zif-8: A comparison of synthesis methods. *Chemical Engineering Journal*, 271, 2015.
- [51] Jin Chong Tan et al. Chemical structure, network topology, and porosity effects on the mechanical properties of zeolitic imidazolate frameworks. *PNAS*, 107, 2010.
- [52] Anne Boutin et al. Thermal and mechanical stability of zeolitic imidazolate frameworks polymorphs. *APL Materials*, 2, 2014.
- [53] Thomas D. Bennett et al. Flux melting of metal–organic frameworks. *RSC Chemical Science*, 10, 2019.
- [54] Vinayak B. Kamble et al. Underpinning the conductivity mechanism in wide bandgap metal organic framework through chemical sensing. *AIP Advances*, 10, 2020.
- [55] Limin Wang et al. Metal organic frameworks route to in situ insertion of multiwalled carbon nanotubes in co₃o₄ polyhedra as anode materials for lithium-ion batteries. *ACS Nano*, 9, 2015.
- [56] Yingjian Yu et al. Zif 8 cooperating in tin/ti/si nanorods as efficient anodes in micro-lithium-ion-batteries. *ACS Applied Materials and Interfaces*, 8, 2016.
- [57] Johan Scheers et al. Benzimidazole and imidazole lithium salts for battery electrolytes. *Journal of Power Sources*, 195, 2010.
- [58] Keith T. Butler et al. Electronic structure design for nanoporous, electrically conductive zeolitic imidazolate frameworks. *Journal of Materials Chemistry C*, 5, 2017.
- [59] Michael I. Ojovan. Viscosity and glass transition in amorphous oxides. *Advances in Condensed Matter Physics*, 12, 2008.
- [60] Qiuju Zheng, Yanfei Zhang, Maziar Montazerian, Ozgur Gulbiten, John C. Mauro, Edgar D. Zanotto, and Yuanzheng Yue. Understanding Glass through Differential Scanning Calorimetry. *Chemical Reviews*, 119(13):7848–7939, jul 2019. doi: 10.1021/acs.chemrev.8b00510.

- [61] Yuanzheng Yue. Characteristic temperatures of enthalpy relaxation in glass. *Journal of Non-Crystalline Solids*, 354, 2007.
- [62] John C. Mauro et al. Enthalpy landscapes and the glass transition. *Scientific Modeling and Simulation*, 15, 2008.
- [63] Morrel H. Cohen and David Turnbull. Molecular transport in liquids and glasses. *The Journal of Chemical Physics*, 31, 1959.
- [64] Marcio Luis Ferreira Nascimento. Correlation between conductivity and free volume in rubidium and cesium silicate glasses. *Brazilian Journal of Physics*, 37, 2007.
- [65] Ang Qiao, Thomas D. Bennett, Haizheng Tao, Andraž Krajnc, Gregor Mali, Cara M. Doherty, Aaron W. Thornton, John C. Mauro, G. Neville Greaves, and Yuanzheng Yue. A metal-organic framework with ultrahigh glass-forming ability. *Science Advances*, 4(3), mar 2018. doi: 10.1126/sciadv.aao6827.
- [66] Louis Frentzel-Beyme, Marvin Kloß, Roman Pallach, Soma Salamon, Henning Moldenhauer, Joachim Landers, Heiko Wende, Jörg Debus, and Sebastian Henke. Porous purple glass—a cobalt imidazolate glass with accessible porosity from a meltable cobalt imidazolate framework. *Journal of Materials Chemistry A*, 7(3):985–990, 2019. doi: 10.1039/c8ta08016j.
- [67] Anonymous. Basics of electrochemical impedance spectroscopy. *Gamry Instruments*.
- [68] Hugo E. Gottlieb, Vadim Kotlyar, and Abraham Nudelman. NMR chemical shifts of common laboratory solvents as trace impurities. *Journal of Organic Chemistry*, 62(21):7512–7515, 1997. doi: 10.1021/jo971176v.
- [69] J. C. Wren et al. Comparative study of film formation on high-purity co and stellite-6: Probing the roles of a chromium oxide layer and gamma-radiation. *Corrosion Science*, 63, 2012.
- [70] Mark C. Biesinger et al. Resolving surface chemical states in xps analysis of first row transition metals, oxides and hydroxides: Cr, mn, fe, co and ni. *Applied Surface Science*, 257, 2011.
- [71] R. I. R. Blyth et al. Xps studies of graphite electrode materials for lithium ion batteries. *Applied Surface Science*, 167, 2000.
- [72] R. J. J. Jansen and H. Van Bekkum. Xps of nitrogen-containing functional groups on activated carbon. *Carbon*, 33, 1994.
- [73] A.L. Greer. Metallic Glasses. In *Encyclopedia of Materials: Science and Technology*, pages 5529–5537. Elsevier, 2001. doi: 10.1016/B0-08-043152-6/00967-0.